On the kinematics of cold, metal-enriched galactic fountain flows in nearby star-forming falaxies

Rubin, K.H.R.; Juarez, C.; Cooksey, K.L.; Werk, J.K.; Prochaska, J.X.; O'Meara, J.M.; ... ; Straka, L.A.

Note: To cite this publication please use the final published version (if applicable).

On the Kinematics of Cold, Metal-enriched Galactic Fountain Flows in Nearby Star-forming Galaxies

Kate H. R. Rubin[1,2] , Christian Juarez[1], Kathy L. Cooksey[3] , Jessica K. Werk[4] , J. Xavier Prochaska[5,6,7] ,
John M. O'Meara[8] , Joseph N. Burchett[9] , Ryan J. Rickards Vaught[2] , Varsha P. Kulkarni[10] , and Lorrie A. Straka[11]

[1] Department of Astronomy, San Diego State University, San Diego, CA 92182 USA; krubin@sdsu.edu
[2] Center for Astrophysics and Space Sciences, Department of Physics, University of California, San Diego, 9500 Gilman Dr., La Jolla, CA 92093, USA
[3] Department of Physics and Astronomy, University of Hawai'i at Hilo, Hilo, HI 96720, USA
[4] Department of Astronomy, University of Washington, Seattle, WA 98195-1580, USA
[5] Department of Astronomy & Astrophysics, University of California, 1156 High Street, Santa Cruz, CA 95064, USA
[6] University of California Observatories, Lick Observatory, 1156 High Street, Santa Cruz, CA 95064, USA
[7] Kavli Institute for the Physics and Mathematics of the Universe (WIP), 5-1-5 Kashiwanoha, Kashiwa, 277-8583, Japan
[8] W.M. Keck Observatory, 65-1120 Mamalahoa Highway, Kamuela, HI 96743, USA
[9] New Mexico State University, Department of Astronomy, Las Cruces, NM 88001, USA
[10] Department of Physics and Astronomy, University of South Carolina, Columbia, SC 29208, USA
[11] Leiden Observatory, Leiden University, PO Box 9513, NL-2300 RA Leiden, The Netherlands
Received 2021 November 24; revised 2022 June 1; accepted 2022 June 20; published 2022 September 12

Abstract

We use medium-resolution Keck/Echellette Spectrograph and Imager spectroscopy of bright quasars to study cool gas traced by Ca II $\lambda\lambda$3934, 3969 and Na I $\lambda\lambda$5891, 5897 absorption in the interstellar/circumgalactic media of 21 foreground star-forming galaxies at redshifts $0.03 < z < 0.20$ with stellar masses $7.4 \leqslant \log M_*/M_\odot \leqslant 10.6$. The quasar–galaxy pairs were drawn from a unique sample of Sloan Digital Sky Survey quasar spectra with intervening nebular emission, and thus have exceptionally close impact parameters ($R_\perp < 13$ kpc). The strength of this line emission implies that the galaxies' star formation rates (SFRs) span a broad range, with several lying well above the star-forming sequence. We use Voigt profile modeling to derive column densities and component velocities for each absorber, finding that column densities $N(\text{Ca II}) > 10^{12.5}\,\text{cm}^{-2}$ ($N(\text{Na I}) > 10^{12.0}\,\text{cm}^{-2}$) occur with an incidence $f_C(\text{Ca II}) = 0.63^{+0.10}_{-0.11}$ ($f_C(\text{Na I}) = 0.57^{+0.10}_{-0.11}$). We find no evidence for a dependence of f_C or the rest-frame equivalent widths $W_r(\text{Ca II K})$ or $W_r(\text{Na I 5891})$ on $R_\perp$ or M_*. Instead, $W_r(\text{Ca II K})$ is correlated with local SFR at $>3\sigma$ significance, suggesting that Ca II traces star formation-driven outflows. While most of the absorbers have velocities within ± 50 km s^{-1} of the host redshift, their velocity widths (characterized by Δv_{90}) are universally 30–177 km s^{-1} larger than that implied by tilted-ring modeling of the velocities of interstellar material. These kinematics must trace galactic fountain flows and demonstrate that they persist at $R_\perp > 5$ kpc. Finally, we assess the relationship between dust reddening and $W_r(\text{Ca II K})$ ($W_r(\text{Na I 5891})$), finding that 33% (24%) of the absorbers are inconsistent with the best-fit Milky Way $E(B-V)$-W_r relations at $>3\sigma$ significance.

Unified Astronomy Thesaurus concepts: Galaxies (573); Quasar-galaxy pairs (1316); Interstellar medium (847); Circumgalactic medium (1879); Quasar absorption line spectroscopy (1317)

Supporting material: machine-readable tables

1. Introduction

The disk–halo interface is host to diverse baryonic processes that regulate the buildup of stellar mass in star-forming galaxies (Shapiro & Field 1976; Bregman 1980; Norman & Ikeuchi 1989; de Avillez 2000). Supernova activity in galactic disks generate wind-blown bubbles in the interstellar medium (ISM; Mac Low & McCray 1988; Tenorio-Tagle & Bodenheimer 1988; Korpi et al. 1999), some of which are sufficiently powerful to evacuate thermalized supernova ejecta and entrain cold material through this interface into the circumgalactic medium (CGM; e.g., Tomisaka & Ikeuchi 1986; Veilleux et al. 1995; Cooper et al. 2008; Fielding et al. 2018). At the same time, the material required to feed ongoing star formation must likewise pass through this region, originating either beyond or in distant regions of the galactic halo, or condensing from

previously ejected stellar and interstellar material (e.g., Lehner & Howk 2011; Marasco et al. 2012; Kim & Ostriker 2018).

In the Milky Way, disk–halo material is observed in emission across a broad range of phases, including hot, diffuse gas traced by X-ray emission (Egger & Aschenbach 1995; Kerp et al. 1999; Kuntz & Snowden 2000), a warm, denser phase traced by Hα emission (e.g., Weiner & Williams 1996; Bland-Hawthorn et al. 1998; Haffner et al. 2003), the cool, neutral material that emits at 21 cm (e.g., Bajaja et al. 1985; Wakker & van Woerden 1991; Kalberla et al. 2005; McClure-Griffiths et al. 2009), and a subdominant cold phase arising in molecular clouds (Gillmon & Shull 2006; Heyer & Dame 2015; Röhser et al. 2016). Gas with temperatures spanning much of this range has likewise been observed in metal-line absorption toward distant QSOs or UV-bright Galactic stars (e.g., Richter et al. 2001a, 2001b; Wakker 2001; Howk et al. 2003; Yao et al. 2009; Lehner & Howk 2011; Werk et al. 2019). Indeed, detection of absorption due to the Ca II $\lambda\lambda$3934, 3969 and Na I $\lambda\lambda$5891, 5897 transitions toward stars in the Galactic disk and halo provided the first evidence for the existence of the ISM (e.g., Hartmann 1904; Hobbs 1969, 1974), and for the presence

of interstellar material above the Galactic plane (Münch & Zirin 1961). The propensity of these transitions to arise in warm (temperature $T < 10,000$ K) and cold ($T < 1000$ K) gas phases, respectively, make them effective tracers of the neutral ISM (Crawford 1992; Welty et al. 1996; Richter et al. 2011; Puspitarini & Lallement 2012).

Over the past several decades, detailed study of these absorption transitions have, e.g., provided important constraints on the distances and temperatures of massive H I cloud complexes (Wakker 2001; Ben Bekhti et al. 2008, 2012), revealed the small-scale structure of neutral material in the Milky Way halo (Smoker et al. 2015; Bish et al. 2019), and placed novel constraints on the physics and composition of interstellar dust (e.g., Phillips et al. 1984; Sembach & Danks 1994; Welty et al. 1996; Murga et al. 2015). The comprehensive analysis of Ca II and Na I transitions in several hundred QSO spectra by Ben Bekhti et al. (2012) demonstrated that this absorption has comparable Milky Way sky coverage to that of H I detected in emission, and that approximately half of the absorber sample have positions and velocities consistent with those of known H I complexes.

Absorption from Ca II is also known to trace cool circumgalactic material in the halos of external galaxies. Several studies have used spectroscopy of background QSO sight lines to identify this transition in association with known foreground systems, reporting detections within projected separations $R_\perp \lesssim 30$ kpc (e.g., Boksenberg & Sargent 1978; Boksenberg et al. 1980; Blades et al. 1981; Bergeron et al. 1987; Zych et al. 2007). Taking advantage of Sloan Digital Sky Survey (SDSS) spectroscopy of more than 100,000 quasars, Zhu & Ménard (2013) analyzed the mean Ca II signal induced as a function of projected separation from nearly one million foreground galaxies, tracing significantly detected absorption from $R_\perp \sim 7$ to 200 kpc. Detections of circumgalactic Na I, on the other hand, have been rarer: prior to the advent of the SDSS, fewer than 10 galaxy–absorber pairs, all within $R_\perp < 15$ kpc, were reported in the literature (e.g., Bergeron et al. 1987; Womble et al. 1990; Stocke et al. 1991; Richter et al. 2011). The mining of SDSS QSO spectra for individual Na I systems increased this sample by a modest factor (e.g., Cherinka & Schulte-Ladbeck 2011; York et al. 2012; Straka et al. 2015); however, the limited signal-to-noise and spectral resolution of these data are ill-suited to detailed study of either of these transitions in individual QSO sight lines. Instead, Na I absorption has long been leveraged to study ISM kinematics in "down-the-barrel" galaxy spectroscopy, revealing ubiquitous, large-scale outflows in massive, starbursting and active galactic nucleus (AGN)–host systems (e.g., Heckman et al. 2000; Martin 2005; Rupke et al. 2005, 2017; Veilleux et al. 2020; Rupke et al. 2021), as well as in more typical star-forming galaxies with stellar masses $10 < \log M_*/M_\odot < 11$ (Chen et al. 2010b; Concas et al. 2019; Roberts-Borsani et al. 2020).

In this work, we use medium-resolution ($\mathcal{R} \approx 8000$) optical spectroscopy of 21 bright quasars confirmed to lie exceptionally close to known foreground systems at redshifts $0.03 < z < 0.20$ to study cold ($T \lesssim 10,000$ K) disk–halo material traced by Ca II $\lambda\lambda 3934, 3969$ and Na I $\lambda\lambda 5891, 5897$ absorption. These sight lines were drawn from a unique sample of quasars surveyed by the SDSS, for which unassociated foreground nebular emission lines were identified in their SDSS fiber spectra. These systems, called Galaxies on Top of Quasars (or GOTOQs), were first discovered by Noterdaeme et al. (2010), and later studies have since uncovered a sample of 103 such objects (York et al. 2012; Straka et al. 2013, 2015). Kulkarni et al. (2022) recently presented Hubble Space Telescope Cosmic Origins Spectrograph data for eight GOTOQs (including five in the present study), confirming that these systems give rise to damped or subdamped Lyα absorption in all cases. Straka et al. (2015) performed photometric analysis of the SDSS imaging of the full sample of 103 pairs, constraining galaxy luminosities, stellar masses, and impact parameters ($R_\perp$), and used emission-line fluxes measured from the SDSS spectroscopy to assess the galaxies' star formation activity at the location of the fiber. Here we combine these measurements with our sensitive follow-up optical spectroscopy to explore the incidence and kinematics of Ca II and Na I absorption within $R_\perp < 13$ kpc of a sample of external galaxies for the first time. We use our sample to trace the dependence of the absorption strengths of these transitions on the stellar masses (M_*) and local star formation rates (SFRs) of the foreground host systems, as well as their relationship to the dust reddening along the sight lines. The relatively high (echellette) spectral resolution of our data set, in combination with the uniquely small impact parameters of the QSOs we target, permit novel insights into the ubiquity of galactic fountain flows in the nearby star-forming galaxy population.

We describe our sample selection and echellette spectroscopy in Section 2, and describe salient properties of the foreground host galaxies in our sample as measured by Straka et al. (2015) in Section 3. We detail our methods of measuring foreground galaxy redshifts and absorption-line equivalent widths, column densities, and kinematics in Section 4. Section 5 presents our results on the relationship between these absorption-line properties and $R_\perp$, dust reddening, foreground galaxy M_*, and local SFR. In Section 6, we develop a simple model of the Ca II- and Na I-absorbing properties of the Milky Way's ISM and demonstrate that such a model fails to explain the large column densities and kinematic widths we measure. We discuss the implications of these findings in light of complementary studies of Ca II and Na I absorption detected toward background QSO sight lines and in down-the-barrel galaxy spectroscopy in Section 7. We adopt a Λ cold dark matter cosmology with $H_0 = 70$ km s^{-1} Mpc^{-1}, $\Omega_M = 0.3$, and $\Omega_\Lambda = 0.7$. Magnitudes quoted are in the AB system.

2. Sample Selection and Observations

Our target quasar sample is drawn from the parent sample of 103 GOTOQs discovered in SDSS spectra by Noterdaeme et al. (2010), York et al. (2012), Straka et al. (2013), and Straka et al. (2015). The latter study performed photometric analysis of the SDSS imaging of all QSO-galaxy pairs, measuring galaxy luminosities, impact parameters, and stellar masses. They also calculated SFRs from the extinction-corrected Hα and [O II] luminosities measured within the SDSS fiber spectroscopy of the background QSOs. The intervening galaxies in this parent sample span a range of redshifts $0 < z < 0.84$, have impact parameters 0.4 kpc $< R_\perp < 12.7$ kpc, and span a wide range in stellar mass ($7.3 < \log M_*/M_\odot < 11.5$).

We used the following criteria to select targets for follow-up echellette-resolution spectroscopy: (1) a continuum-emitting counterpart to the foreground system was identified by Straka et al. (2015); (2) the foreground galaxy redshift must be such that the Na I D doublet falls outside of spectral regions with significant atmospheric absorption (at observed wavelengths

Table 1
Observed GOTOQ Sample

Sight Line	R.A. (J2000)	Decl. (J2000)	z_{QSO}[i]	$z_{H\alpha}$[ii]	$R_\perp$[i] (kpc)	m_r(QSO)[i] (mag)	$\log M_*/M_\odot$[i]	SFR(Hα)[i] ($M_\odot$ yr^{-1})	$E(B-V)_{(g-i)}$[i] (mag)
GOTOQJ0013−0024	00:13:42.45	−00:24:12.60	1.641	0.15537	3.40	18.58	10.4	60.30	0.24
GOTOQJ0851+0719	08:51:13.74	+07:19:59.80	1.650	0.13010	5.63	17.97	8.4	0.35	−0.06
GOTOQJ0902+1414[iii]	09:02:50.47	+14:14:08.29	0.980	0.05044	3.59	18.43	9.7	0.03	0.05
GOTOQJ0950+5442[iii]	09:50:13.74	+54:42:54.65	0.700	0.04586	0.98	18.33	8.8	⋯	−0.09
GOTOQJ1005+5302	10:05:14.21	+53:02:40.04	0.560	0.13547	3.60	18.79	9.6	0.19	−0.15
GOTOQJ1044+0518[iii]	10:44:30.26	+05:18:57.32	0.900	0.10781	3.51	17.77	8.8	0.54	0.21
GOTOQJ1135+2414[iii]	11:35:55.66	+24:14:38.10	1.450	0.03426	3.88	19.22	9.4	0.01	−0.10
GOTOQJ1158+3907[iii]	11:58:22.85	+39:07:12.96	1.160	0.18337	4.66	18.04	7.4	0.15	0.07
GOTOQJ1220+2837	12:20:37.23	+28:37:52.03	2.200	0.02762	6.88	17.91	8.7	⋯	0.04
GOTOQJ1238+6448	12:38:46.68	+64:48:36.60	1.560	0.11859	7.00	17.93	7.7	2.21	0.10
GOTOQJ1241+6332	12:41:57.55	+63:32:41.63	2.620	0.14270	10.57	17.96	10.6	0.40	0.22
GOTOQJ1248+4035	12:48:14.43	+40:35:35.13	2.110	0.15132	4.00	19.11	10.2	⋯	0.12
GOTOQJ1328+2159	13:28:24.33	+21:59:19.66	0.330	0.13524	12.68	18.96	9.1	0.16	−0.16
GOTOQJ1429+0120	14:29:17.69	+01:20:58.93	1.130	0.08395	3.43	18.70	9.9	0.11	0.13
GOTOQJ1457+5321[iii]	14:57:19.00	+53:21:59.27	1.200	0.06594	4.24	18.16	9.3	0.04	0.00
GOTOQJ1459+3713	14:59:38.50	+37:13:14.70	1.220	0.14866	4.40	19.02	9.6	3.55	−0.04
GOTOQJ1525+0202[iii]	15:25:14.08	+02:02:54.68	1.220	0.09019	3.12	18.73	8.3	⋯	0.14
GOTOQJ1605+5107	16:05:21.26	+51:07:40.95	1.230	0.09899	3.80	18.58	9.3	0.19	0.19
GOTOQJ1656+2541	16:56:43.35	+25:41:36.80	0.243	0.03451	1.13	18.16	8.9	0.03	0.42
GOTOQJ1659+6202	16:59:58.94	+62:02:18.14	0.230	0.11026	7.15	17.80	9.8	0.26	−0.03
GOTOQJ1717+3203	17:17:04.14	+32:03:20.93	0.660	0.20016	7.51	18.68	9.9	1.15	0.00

Notes.

[i] These quantities are drawn from the analysis of Straka et al. (2015). Values of $\log M_*/M_\odot$ and SFR(Hα) were calculated for the foreground galaxy. As discussed in Section 3, the latter estimates should be considered lower limits due to the likelihood of fiber losses, and are referred to as SFR$_{local}$ throughout the text. Values of $E(B-V)_{(g-i)}$ refer to the background QSO and are estimated by comparing each QSO's $(g-i)$ color to the median $(g-i)$ color for QSOs at the same redshift as reported in Schneider et al. (2007).

[ii] This is the foreground galaxy redshift calculated as described in Section 4.1.

[iii] For this sight line, we use the SDSS spectrum rather than the ESI spectrum to determine a precise emission-line redshift.

(This table is available in machine-readable form.)

$\lambda_{obs} = 6850$–$6950\,\text{Å}$ and 7580–$7710\,\text{Å}$); and (3) the quasar must be sufficiently bright to yield a 2σ rest equivalent width (W_r) detection limit of $\approx 0.02\,\text{Å}$ at $\lambda_{obs} = 6000$–$7500\,\text{Å}$ in an exposure time of $\leqslant 1$ hr. This latter constraint corresponds to an r-band magnitude limit of $m_r \lesssim 19.1$ for the background quasar. Approximately 36 GOTOQs in the Straka et al. (2015) parent sample satisfy all of these criteria. We completed follow-up spectroscopy of 21 of these targets. Table 1 lists their coordinates, as well as the QSO redshifts, impact parameters, and other properties of the foreground galaxies as reported in Straka et al. (2015). SDSS color images of each system are included in Figure 1.

Our observations were carried out using the Echellette Spectrograph and Imager (ESI; Sheinis et al. 2002) on the Keck II Telescope on 2017 March 6 UT and 2017 June 22–23 UT. Seeing conditions ranged between FWHM $\sim 0\rlap{.}''4$–$0\rlap{.}''8$ over the course of the program. We used the $0\rlap{.}''5$ wide longslit with ESI, which affords an FWHM resolution of $\mathcal{R} \approx 8000$ ($37.3\,\text{km s}^{-1}$), a spectral dispersion of $10\,\text{km s}^{-1}$, and a typical wavelength coverage of 3990–$10130\,\text{Å}$. We exposed for between 20 and 70 minutes total per object, dividing each observation into two to four individual exposures.

The data were reduced using the XIDL ESIRedux data reduction pipeline.[12] The pipeline includes bias subtraction, flat-fielding, wavelength calibration, the tracing of order curvature, object identification, sky subtraction, cosmic-ray

rejection, and relative flux calibration. We also used it to apply a vacuum and heliocentric correction to each spectrum.

3. Foreground Galaxy Properties

For this analysis, we draw on stellar mass estimates reported by Straka et al. (2015) for the parent GOTOQ sample. Stellar masses were determined via spectral energy distribution (SED) model fits to photometry of the host galaxies measured in the five SDSS passbands with the photometric redshift code HYPERZ (Bolzonella et al. 2000; Straka et al. 2015). The left panel of Figure 2 shows the $\log M_*/M_\odot$ distribution of our foreground host sample versus $R_\perp$. These systems span an overall wide range of stellar masses ($7.4 \leq \log M_*/M_\odot \leq 10.6$), with a median $\log M_*/M_\odot = 9.3$. Our sight lines sample this parameter space relatively thoroughly within $R_\perp < 9$ kpc; however, we caution that our constraints beyond $R_\perp > 10$ kpc are sparse.

Under the assumption that the absorption strength of our transitions of interest at a given $R_\perp$ may depend on the relative extent of a galaxy's stellar component, we use the observed relation between M_* and effective radius (R_{eff}) for late-type galaxies to estimate R_{eff} for each host. We use the best-fit R_{eff}-M_* relation estimated by van der Wel et al. (2014) for systems having $0 < z < 0.5$:

$$R_{eff,est} = 10^{0.86}\left(\frac{M_*}{5 \times 10^{10} M_\odot}\right)^{0.24} \text{kpc}. \qquad (1)$$

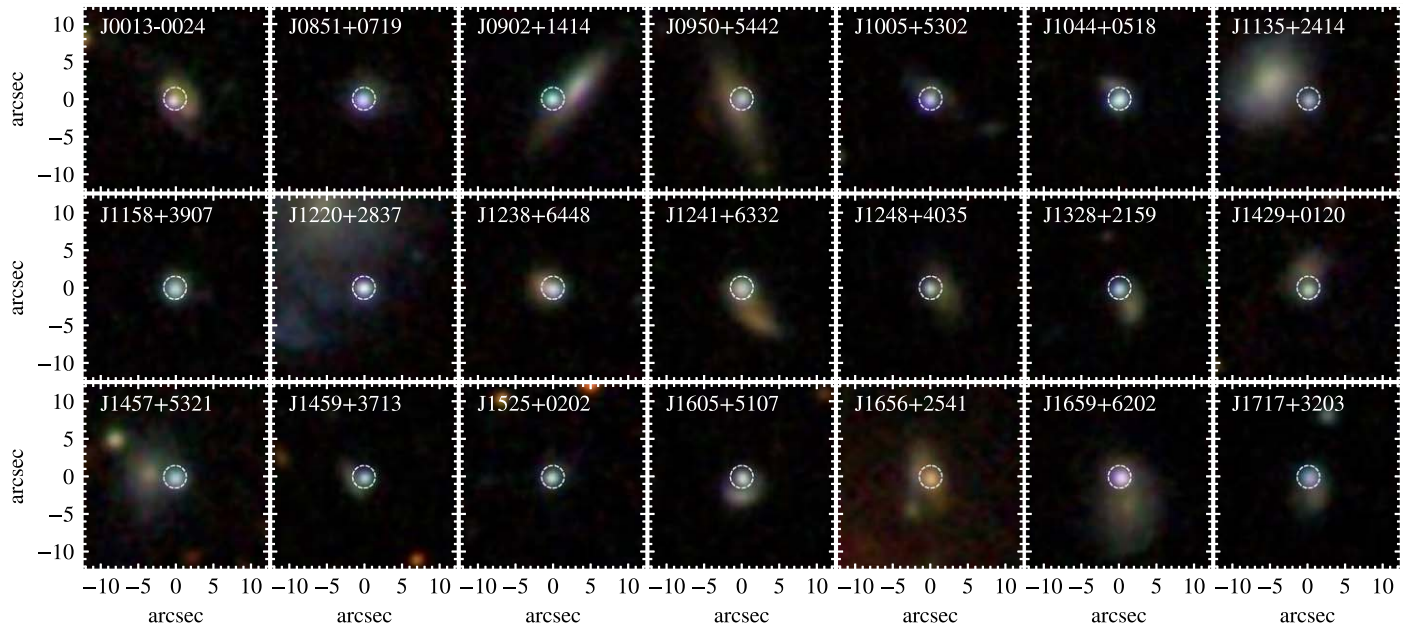[12] https://www2.keck.hawaii.edu/inst/esi/ESIRedux/

Figure 1. SDSS *gri* color imaging of all GOTOQs for which we have obtained Echellette Spectrograph and Imager (ESI) spectroscopy (York et al. 2000). Each panel is $25'' \times 25''$. The images are labeled with the corresponding GOTOQ ID at the upper left. The dashed white circle indicates the size of the $3''$ diameter fiber used for the SDSS spectroscopy of each system.
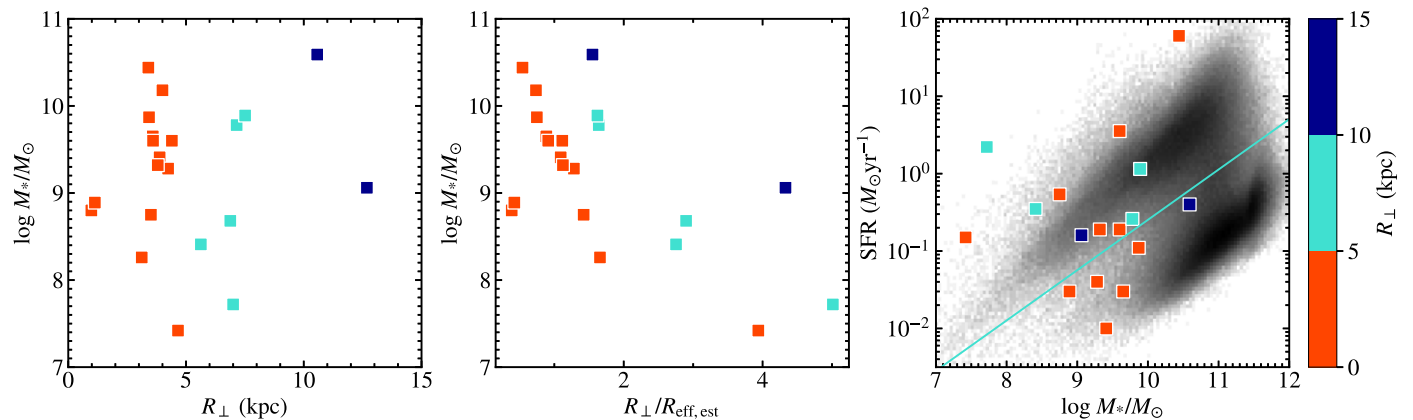

Figure 2. Left: distribution of $\log M_*/M_\odot$ vs. $R_\perp$ for our sample. Points are color-coded by the $R_\perp$ value for each system across all panels, as indicated by the color bar at right. Middle: distribution of $\log M_*/M_\odot$ vs. $R_\perp/R_{\rm eff,est}$ for our foreground GOTOQ sample. Right: distribution of SFR$_{\rm local}$ vs. $\log M_*/M_\odot$ for our foreground GOTOQ sample. The SFR values shown here should be considered lower limits on the total SFR of each system due to fiber losses. The grayscale histogram shows the distribution of total SFR versus M_* for all galaxies included in the MPA-JHU catalog of these values for SDSS DR7 (Brinchmann et al. 2004). The turquoise line shows a linear fit to the minimum in the galaxy distribution between star-forming and quiescent systems by Moustakas et al. (2013) for $z = 0$.

These values fall in the range $1.2\,{\rm kpc} \lesssim R_{\rm eff,est} \lesssim 6.8\,{\rm kpc}$ for our sample. These authors also assess the intrinsic scatter in this relation, estimating $\sigma(\log R_{\rm eff}) = 0.16$. The true size of any given galaxy in our sample may therefore differ from this best-fit estimated size by a few kiloparsecs; however, we note that estimates of galaxy halo virial radii (often used in CGM studies in the same way we will use $R_{\rm eff,est}$ below) are typically subject to a greater degree of uncertainty. We normalize the $R_\perp$ value for each system by its $R_{\rm eff,est}$ estimate and compare this quantity to $\log M_*/M_\odot$ in the middle panel of Figure 2. Due to the correlation between M_* and $R_{\rm eff,est}$, the sight lines with $R_\perp/R_{\rm eff,est} > 2$ tend to probe the lower-M_* hosts in our sample (i.e., those with $\log M_*/M_\odot \lesssim 9$).

We likewise make use of the SFRs estimated by Straka et al. (2015) for these systems from the extinction-corrected Hα luminosities measured in the SDSS fiber spectra. Extinction

corrections were determined from the ratio of Hα to Hβ line luminosities and adopted an SMC extinction curve (Straka et al. 2015). The Kennicutt (1998) empirical calibration was then applied to the intrinsic Hα luminosities. As noted by Straka et al. (2015), because the SDSS fibers used to observe these galaxies were typically placed such that a significant fraction of their Hα line emission was lost (see Figure 1), these SFRs should be considered lower limits on the total star formation activity of the hosts. Moreover, the fraction of line emission missed by the fiber is likely larger for systems with larger impact parameters. We explore this effect in Appendix A, modeling the distribution of star formation in each foreground system as an exponential disk with a scale radius consistent with $R_{\rm eff,est}$. This simple analysis implies that the SDSS fibers capture $\gtrsim 10\%$ of the Hα emitted by the majority of the galaxies probed within $R_\perp < 5$ kpc, but may miss $\gtrsim 90\%$–99% of the Hα emission from systems at larger spatial offsets. The measured Hα luminosities and SFRs instead provide accurate

assessments of the star formation activity close to the absorbing material detected along our QSO sight lines (i.e., the "local" SFR). For this reason, we refer to this quantity as $\text{SFR}_{\text{local}}$ below.

The distribution of $\text{SFR}_{\text{local}}$ and $\log M_*/M_\odot$ values for our foreground galaxy sample is shown in the rightmost panel of Figure 2 with colored points. The grayscale histogram shows the distribution of *total* SFR and $\log M_*/M_\odot$ for the SDSS DR7 galaxy population (Brinchmann et al. 2004). The turquoise curve shows a linear fit to the minimum in the bimodal galaxy distribution estimated by Moustakas et al. (2013) and extrapolated to $z = 0$. Several of our foreground galaxies lie below this line, in the parameter space primarily occupied by non-star-forming, early-type systems. This is likely because we have not measured their total, integrated SFRs (as described above). The modeling we perform in Appendix A implies that all of our systems likely have total SFRs $> 0.1 \, M_\odot \, \text{yr}^{-1}$, and that those systems with $R_\perp > 5 \, \text{kpc}$ may have total SFRs $\gtrsim 10 \, M_\odot \, \text{yr}^{-1}$. The latter galaxies should therefore be considered starbursting systems. The location of our sample in this parameter space may likewise be affected by overestimation of the galaxy stellar masses due to systematics associated with SED modeling of the shallow SDSS photometry. The 1σ uncertainty intervals for the $\log M_*/M_\odot$ values reported by Straka et al. (2015) for our sample have a mean of 0.54 dex, and range up to 2.0 dex.

4. Line Profile Analysis

4.1. Foreground Galaxy Redshifts

Because we are interested in the detailed kinematic structure of absorption detected along our target sight lines, and because Straka et al. (2015) reported redshifts with only four significant figures, we draw on our ESI spectra to measure more precise redshifts for our GOTOQ sample. We inspected each ESI spectrum for the presence of narrow emission features at the observed wavelengths of $H\alpha$ and [O III] $\lambda 5008$ for the associated foreground galaxy. We identified both transitions in eight sight lines, and identified only $H\alpha$ in an additional six systems. The remaining seven sight lines (indicated with "c" superscripts in Table 1) lack narrow emission features at the expected locations of $H\alpha$ and [O III]; this is most likely because the ESI slit placement was insufficiently close to the foreground system. For these sight lines, we use their SDSS DR16 spectra (York et al. 2000; Ahumada et al. 2020) to reassess the GOTOQ redshift. We determine the continuum level of each QSO by fitting a spline function to feature-free spectral regions using the `lt_continuumfit` graphical user interface (GUI), available with the Python package `linetools`[13] (Prochaska et al. 2016). This tool presents the user with an automatically generated continuum spline, fit to a set of knots whose flux levels are determined from the mean flux in a series of spectral "chunks." We performed a visual inspection of these knots, adjusting their placement in cases where their location was unduly affected by nearby absorption or emission features.

We subtracted this continuum level from each spectrum and performed a Gaussian fit to the residual flux in a spectral region within either $\pm 300 \, \text{km s}^{-1}$ (for ESI spectra) or $\pm 600 \, \text{km s}^{-1}$ (for the SDSS spectra) of the observed wavelength of $H\alpha$. We used the Levenberg-Marquardt least-squares fitter available within the

`astropy.modeling` package (Astropy Collaboration et al. 2018) to determine the best-fit Gaussian wavelength centroid for this line. The typical magnitude of the redshift uncertainty implied by the covariance matrix for the fitted parameters is $2-5 \, \text{km s}^{-1}$ for the ESI spectra and $4-15 \, \text{km s}^{-1}$ for the SDSS spectra. The fitted redshift values are all within a maximum of $\pm 112 \, \text{km s}^{-1}$ of those published for the foreground systems by Straka et al. (2015). We refer to the redshifts determined via this method as $z_{H\alpha}$ in the following text.

4.2. Absorption-line Profile Characterization and Modeling

We then characterized the absorption strength and kinematics of the Ca II H & K and Na I transitions associated with each GOTOQ. We used the `XAbsSysGui`, available with `linetools`, to perform a visual inspection of these transitions. In cases in which an absorption feature is clearly evident within $\pm 300 \, \text{km s}^{-1}$ of $z_{H\alpha}$, we use this GUI to manually select the velocity window to be used for the computation of the W_r of each line. We also noted the occasional presence of blended absorption features that are unassociated with $z_{H\alpha}$. In cases of transitions lacking clear absorption features, velocity windows were set to $\pm 150 \, \text{km s}^{-1}$ by default, but were adjusted as necessary to exclude unassociated blends. These windows were used to calculate upper limits on W_r. Spectral regions covering the Ca II H & K and Na I doublet transitions in the rest frame of the corresponding foreground galaxies for five systems in our sample are shown in Figure 3. Similar figures showing the remaining sight lines are included in Appendix B. Our ESI spectra have signal-to-noise ratios (S/Ns) in the range $20-34 \, \text{pix}^{-1}$ with a median $\text{S/N} = 24 \, \text{pix}^{-1}$ within $\lesssim 400 \, \text{km s}^{-1}$ of the GOTOQ Na I transitions. The spectral S/N within $200-400 \, \text{km s}^{-1}$ of the Ca II K transitions ranges between $2-22 \, \text{pix}^{-1}$, with a median $\text{S/N} = 10 \, \text{pix}^{-1}$.

We used the velocity windows mentioned above to compute the W_r for each Ca II and Na I transition. For those sight lines yielding a significantly detected W_r in at least one transition, we refer to these absorbers as "systems" in the following. We also used the apparent optical depth method (Savage & Sembach 1991) to compute the column density of each transition and its uncertainty. For those systems in which both doublet lines are significantly detected and unblended, we computed the mean of the column densities of both doublet lines, weighted by their respective uncertainties, and report this value as N_{aod}. For those systems in which only the transition with the larger oscillator strength (Ca II K or Na I 5891) is significantly detected, we adopt its apparent optical depth column density as the value of N_{aod}. For those sight lines in which the stronger line is not detected, we report 3σ upper limits on the column density computed from the apparent optical depth method for the stronger transition only. All velocity limits, W_r and N_{aod} values, and the associated uncertainties (σ_{W_r} and $\sigma_{N_{\text{aod}}}$) are reported in Tables 2 and 3.

Straka et al. (2015) measured unblended $W_r(\text{Na I } 5891)$ values using the corresponding SDSS spectra for 16 of our 21 sight lines: 12 of these are upper limits consistent with our constraints, two are detections consistent with our values, and two of the Straka et al. (2015) $W_r(\text{Na I } 5891)$ values are larger by $1.4-2.6\sigma$. These authors likewise presented measurements of $W_r(\text{Ca II K})$ for each of our sight lines, five of which are upper limits consistent with our constraints. The remainder are detections that are all larger than our measurements, and 10 of these differ by $> 1.0\sigma$. This offset may arise from the use of a larger velocity window by Straka et al. (2015, although the adopted window is not specified in that work) and/or the inclusion of noise features for some systems.
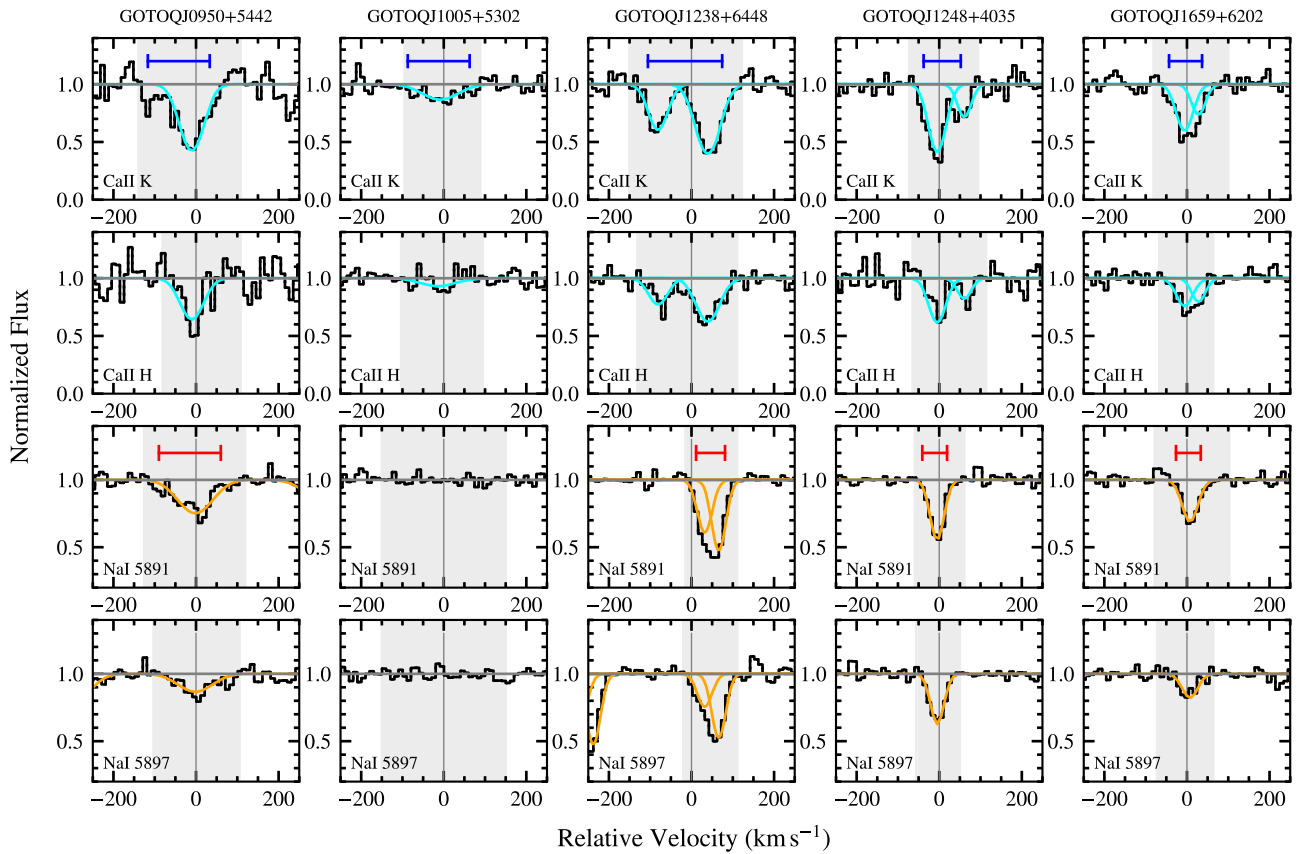
---

[13] https://linetools.readthedocs.io/en/latest/

Figure 3. Regions of five of our ESI GOTOQ spectra showing the locations of Ca II H & K and Na I $\lambda\lambda$5891, 5897 transitions associated with the foreground galaxy. The velocity is defined relative to the GOTOQ redshift estimated from a Gaussian fit to its Hα emission as described in Section 4.1 ($z_{H\alpha}$). The gray horizontal line indicates the continuum level, and the gray shaded region shows the velocity window selected for computation of W_r, N_{aod}, and Δv_{90}. The blue and red bars show the pixels that contain >5% of the total apparent optical depth of the line (determined by stepping inward from the profile edges), and the length of these bars corresponds to Δv_{90}. Best-fit profile models are shown with cyan (for Ca II) and orange (for Na I) curves for systems with significantly detected absorption (see Section 4.2 for details).

We characterize the velocity spread of each significantly detected absorption-line system in a model-independent way using a modified version of the Δv_{90} measurement described in Prochaska & Wolfe (1997). We first smooth the apparent optical depth profile of each system with a boxcar of width = 37.3 km s^{-1} and replace any negative apparent optical depth values with a value of zero. We then step inward from the left and right edges of each profile, summing the apparent optical depths to identify the pixels containing >5% of the integrated optical depth of the system. The corresponding value of Δv_{90} is the velocity width between these left- (at relative velocity $\delta v_{90, \text{left}}$) and rightmost pixels (at relative velocity $\delta v_{90, \text{right}}$). This measurement is listed in Tables 2 and 3, and we make use of both these values and our estimates of $\delta v_{90, \text{left}}$ and $\delta v_{90, \text{right}}$ in the kinematic analyses to follow.

We performed Voigt profile modeling of each significantly detected absorption system using the publicly available `veeper` Python package.[14] The `veeper`, developed by coauthor J. Burchett, determines best-fit values of the column density (N_{vp}), Doppler parameter (b_D), and central velocity relative to $z_{H\alpha}$ (δv) via least-squares minimization. Parameter space was explored using the iterative `MPFIT` software, originally written in IDL by C. Markwardt[15] and then rewritten in Python by M. Rivers.[16] The user sets initial guesses for each parameter by

eye and may then inspect the resulting fit using an interactive GUI. The permitted values of b_D were limited to the range 1 km s^{-1} < b_D < 85 km s^{-1}. Both transitions of each ion were fit simultaneously, and we adopted a Gaussian line spread function with $\sigma = 15.8$ km s^{-1} across the full spectral range. Each absorber was fit twice; once with a single velocity component and, again, with two velocity components initially offset by ±10 km s^{-1}. We adopted the best-fit parameters of the two-component fit if it yielded a lower reduced-χ^2 (χ_r^2) value than the one-component fit and reasonable values for the formal 1σ parameter uncertainties calculated from the covariance matrix (i.e., $\sigma_{\log N_{vp}} < 0.5$). While some of these systems may have more than two absorbing structures along the line of sight, we did not attempt more complex profile modeling (e.g., with three or more components) because we generally achieved low χ^2 values with our one- or two-component fits ($\chi_r^2 = 0.67-4.52$), and because our primary findings and conclusions would not be affected by invoking more complex analyses.

There are two absorption-line systems for which both our one-component and two-component `veeper` fitting fails to yield useful parameter constraints (i.e., $\sigma_{\log N_{vp}} > 1$ or $\sigma_{b_D} > 50$ km s^{-1}): the Ca II absorber toward GOTOQJ1328+2159, and the Na I absorber toward GOTOQJ1429+0120. We posit that this is due to noise features in these profiles that cause the two doublet lines to exhibit unphysical doublet ratios. In these cases, we fix the value of the total column density to N_{aod} and perform a one-component `veeper` fit allowing only the b_D and δv parameters to vary. We also note that the 1σ parameter uncertainties calculated

Table 2
Ca II Absorption-line Equivalent Widths, Kinematics, and Best-fit Voigt Profile Model Parameters

Sight Line	$R_\perp$ (kpc)	W_r(Ca II K)[a] (Å)	Velocity Limits (km s^{-1})	log $N_{\rm aod}$(Ca II)[a] (cm^{-2})	Δv_{90}(Ca II K) (km s^{-1})	log $N_{\rm vp}$(Ca II) (cm^{-2})	$b_{\rm D}$(Ca II) (km s^{-1})	δv(Ca II) (km s^{-1})	χ_r^2(Ca II)
J0013−0024	3.4	0.96 ± 0.07	[−83,131]	13.02 ± 0.09	130	13.17 ± 0.12	⋯	⋯	1.58
		⋯	⋯	⋯	⋯	12.71 ± 0.22	11.4 ± 15.9	−28.5 ± 6.2	⋯
		⋯	⋯	⋯	⋯	12.99 ± 0.15	47.3 ± 17.1	28.1 ± 15.7	⋯
J0851+0719	5.6	<0.12	[−150,150]	<12.14	⋯	⋯	⋯	⋯	⋯
J0902+1414	3.6	<0.20	[−42,70]	<12.41	⋯	⋯	⋯	⋯	⋯
J0950+5442	1.0	0.64 ± 0.08	[−139,108]	12.93 ± 0.05	150	12.96 ± 0.05	29.6 ± 5.1	−6.0 ± 3.1	0.99
J1005+5302	3.6	0.21 ± 0.03	[−95,88]	12.40 ± 0.06	150	12.35 ± 0.07	55.0 ± 11.3	−9.7 ± 7.5	0.98
J1044+0518	3.5	0.32 ± 0.03	[−78,105]	12.56 ± 0.04	100	12.62 ± 0.04	⋯	⋯	1.00
		⋯	⋯	⋯	⋯	11.68 ± 0.20	8.9 ± 42.8	−21.3 ± 11.6	⋯
		⋯	⋯	⋯	⋯	12.57 ± 0.04	20.0 ± 5.1	45.3 ± 2.3	⋯
J1135+2414	3.9	<0.24	[−75,94]	<12.49	⋯	⋯	⋯	⋯	⋯
J1158+3907	4.7	0.15 ± 0.04	[−59,94]	12.27 ± 0.12	100	12.31 ± 0.10	54.0 ± 17.3	63.1 ± 11.6	1.19
J1220+2837	6.9	0.33 ± 0.07	[−50,47]	12.75 ± 0.08	50	12.91 ± 0.14	13.5 ± 6.6	−4.5 ± 3.2	1.33
J1238+6448	7.0	0.86 ± 0.04	[−150,122]	13.11 ± 0.02	180	13.15 ± 0.02	⋯	⋯	0.97
		⋯	⋯	⋯	⋯	12.65 ± 0.04	22.1 ± 4.3	−80.0 ± 2.2	⋯
		⋯	⋯	⋯	⋯	12.98 ± 0.02	30.9 ± 2.5	40.5 ± 1.5	⋯
J1241+6332	10.6	0.65 ± 0.03	[−42,113]	13.03 ± 0.02	80	13.09 ± 0.02	35.8 ± 2.5	33.9 ± 1.6	2.30
J1248+4035	4.0	0.58 ± 0.03	[−73,94]	12.92 ± 0.03	90	13.02 ± 0.05	⋯	⋯	1.65
		⋯	⋯	⋯	⋯	12.89 ± 0.04	17.6 ± 3.1	−3.8 ± 1.4	⋯
		⋯	⋯	⋯	⋯	12.45 ± 0.17	7.2 ± 4.3	61.7 ± 2.7	⋯
J1328+2159	12.7	0.24 ± 0.03	[−42,55]	12.53 ± 0.05	60	⋯[b]	13.3 ± 6.0	7.1 ± 2.8	1.22
J1429+0120	3.4	0.24 ± 0.06	[−48,72]	12.57 ± 0.11	60	12.66 ± 0.20	10.0 ± 8.9	10.4 ± 3.7	1.19
J1457+5321	4.2	<0.20	[−100,119]	<12.39	⋯	⋯	⋯	⋯	⋯
J1459+3713	4.4	<1.05	[−150,150]	<13.47	⋯	⋯	⋯	⋯	⋯
J1525+0202	3.1	<0.21	[−67,150]	<12.38	⋯	⋯	⋯	⋯	⋯
J1605+5107	3.8	0.45 ± 0.08	[−100,41]	12.84 ± 0.07	80	12.86 ± 0.06	26.6 ± 6.9	−16.1 ± 3.9	1.50
J1656+2541	1.1	<0.42	[−59,47]	<12.80	⋯	⋯	⋯	⋯	⋯
J1659+6202	7.2	0.40 ± 0.03	[−81,99]	12.76 ± 0.03	80	12.96 ± 0.19	⋯	⋯	0.83
		⋯	⋯	⋯	⋯	12.63 ± 0.04	15.5 ± 5.1	−4.5 ± 2.3	⋯
		⋯	⋯	⋯	⋯	12.69 ± 0.36	4.0 ± 2.1	29.2 ± 1.6	⋯
J1717+3203	7.5	0.62 ± 0.02	[−114,77]	12.99 ± 0.02	90	13.18 ± 0.06	⋯	⋯	1.09
		⋯	⋯	⋯	⋯	12.52 ± 0.10	19.5 ± 8.3	−30.3 ± 5.6	⋯
		⋯	⋯	⋯	⋯	13.08 ± 0.08	10.0 ± 1.7	11.4 ± 1.9	⋯

Notes. Best-fit Voigt profile model parameters for Ca II systems fit with a single absorbing component are listed in a single table row. For systems fit with two components, we list the total log $N_{\rm vp}$ of the system in the first row for each sight line and include best-fit log $N_{\rm vp}$, $b_{\rm D}$, and δv values for the individual components in the following two rows.

[a] Upper limits are reported at the 3σ level.

[b] To model this absorber, we fixed the column density to the measured value of $N_{\rm aod}$ as described in Section 4.2.

(This table is available in machine-readable form.)

from the covariance matrix for each absorber fit are formally allowed to overlap regions of parameter space that are excluded from exploration during the fitting process. This results in values of $\sigma_{b_{\rm D}} > b_{\rm D}$ for a few of the weaker components in our two-component fits, implying 1σ confidence intervals that extend to negative values. The Doppler parameters are thus not well-constrained in these cases; however, the corresponding uncertainties on log $N_{\rm vp}$ and δv should reflect the distribution of each parameter value that corresponds to a $\Delta\chi^2 = 1$ if all other parameters are allowed to vary to keep the χ^2 as low as possible (i.e., they are "marginalized" uncertainty intervals).

Best-fit Voigt profile models for each securely detected absorber in our sample are shown in Figure 3 and in Appendix B. The resulting best-fit values of each model parameter, along with their uncertainties, are listed in Tables 2 and 3. The two systems for which we adopt a fixed column density in our profile fitting are indicated with a "b" superscript in the log $N_{\rm vp}$ table columns. We will primarily use our $N_{\rm vp}$ values where available in the analysis to follow. We note that while the values of log $N_{\rm aod}$ and the total log $N_{\rm vp}$ (summed over all components) are universally within ± 0.2 dex for all of our Ca II absorbers and for the vast majority of our Na I systems, there are three sight lines for which the total log $N_{\rm vp}$(Na I) exceeds log $N_{\rm aod}$(Na I) by 0.35–0.66 dex (J1238+6448, J1248 +4035, and J1717+3203). As these absorbers are among the strongest systems in our sample, these offsets are likely due to saturation effects.

5. Ca II and Na I Absorption Properties of the Disk–Halo Interface

Here we examine the incidence of Ca II and Na I absorption in the disk–halo environment and assess the relation between their absorption strengths and $R_\perp$.

5.1. log W_r–$R_\perp$ Relations

We show our measurements of the total system W_r(Ca II K) and W_r(Na I 5891) versus $R_\perp$ in Figure 4 with colored points. Detections and 3σ upper limits on W_r for these transitions measured from SDSS spectra of the parent GOTOQ sample by

Table 3
Na I Absorption-line Equivalent Widths, Kinematics, and Best-fit Voigt Profile Model Parameters

Sight Line	$R_\perp$ (kpc)	W_r(Na I 5891)[a] (Å)	Velocity Limits (km s^{-1})	$\log N_{aod}$(Na I)[a] (cm^{-2})	Δv_{90}(Na I 5891) (km s^{-1})	$\log N_{vp}$(Na I) (cm^{-2})	b_D(Na I) (km s^{-1})	δv(Na I) (km s^{-1})	χ_r^2(Na I)
J0013–0024	3.4	0.62 ± 0.03	[−60,98]	12.60 ± 0.02	100	12.78 ± 0.07	⋯	⋯	0.67
		⋯	⋯	⋯	⋯	12.37 ± 0.05	25.0 ± 5.8	−10.2 ± 3.6	⋯
		⋯	⋯	⋯	⋯	12.57 ± 0.10	5.4 ± 1.9	36.8 ± 2.1	⋯
J0851+0719	5.6	<0.12	[−150,150]	<11.80	⋯	⋯	⋯	⋯	⋯
J0902+1414	3.6	0.21 ± 0.03	[−40,90]	12.11 ± 0.05	60	12.34 ± 0.09	6.4 ± 1.5	1.4 ± 1.6	0.89
J0950+5442	1.0	0.50 ± 0.05	[−125,119]	12.46 ± 0.03	150	12.46 ± 0.03	52.1 ± 5.3	−2.8 ± 3.5	0.92
J1005+5302	3.6	<0.12	[−150,150]	<11.78	⋯	⋯	⋯	⋯	⋯
J1044+0518	3.5	<0.10	[−150,150]	<11.69	⋯	⋯	⋯	⋯	⋯
J1135+2414	3.9	<0.10	[−100,47]	<11.71	⋯	⋯	⋯	⋯	⋯
J1158+3907	4.7	<0.10	[−81,99]	<11.69	⋯	⋯	⋯	⋯	⋯
J1220+2837	6.9	0.79 ± 0.02	[−61,72]	12.74 ± 0.01	70	12.87 ± 0.02	18.3 ± 1.1	−7.8 ± 0.5	4.52
J1238+6448	7.0	0.73 ± 0.03	[−14,111]	12.75 ± 0.01	70	13.41 ± 0.27	⋯	⋯	0.80
		⋯	⋯	⋯	⋯	12.44 ± 0.06	10.5 ± 3.4	33.0 ± 1.5	⋯
		⋯	⋯	⋯	⋯	13.36 ± 0.31	6.0 ± 1.1	67.0 ± 0.7	⋯
J1241+6332	10.6	0.85 ± 0.03	[−61,122]	12.76 ± 0.01	100	12.84 ± 0.01	⋯	⋯	2.57
		⋯	⋯	⋯	⋯	11.99 ± 0.05	16.6 ± 3.8	−16.0 ± 2.0	⋯
		⋯	⋯	⋯	⋯	12.77 ± 0.01	23.6 ± 1.0	50.0 ± 0.6	⋯
J1248+4035	4.0	0.36 ± 0.02	[−59,61]	12.40 ± 0.02	60	12.75 ± 0.05	7.0 ± 0.5	−1.3 ± 0.5	0.87
J1328+2159	12.7	0.11 ± 0.04	[−39,97]	11.79 ± 0.14	70	11.73 ± 0.11	13.0 ± 15.3	6.3 ± 5.7	0.83
J1429+0120	3.4	0.18 ± 0.02	[−39,63]	12.09 ± 0.04	50	⋯[b]	10.1 ± 5.1	−2.4 ± 2.0	1.32
J1457+5321	4.2	0.26 ± 0.04	[−95,86]	12.16 ± 0.07	100	12.12 ± 0.06	36.6 ± 8.2	−26.3 ± 4.9	0.89
J1459+3713	4.4	<0.14	[−150,150]	<11.86	⋯	⋯	⋯	⋯	⋯
J1525+0202	3.1	<0.14	[−150,150]	<11.85	⋯	⋯	⋯	⋯	⋯
J1605+5107	3.8	0.26 ± 0.04	[−89,99]	12.21 ± 0.05	90	12.23 ± 0.08	9.1 ± 5.4	3.3 ± 1.9	1.16
J1656+2541	1.1	<0.12	[−50,150]	<11.77	⋯	⋯	⋯	⋯	⋯
J1659+6202	7.2	0.24 ± 0.03	[−78,102]	12.17 ± 0.04	60	12.28 ± 0.03	13.8 ± 3.5	6.3 ± 1.4	0.89
J1717+3203	7.5	0.65 ± 0.03	[−78,80]	12.71 ± 0.01	60	13.16 ± 0.11	⋯	⋯	1.06
		⋯	⋯	⋯	⋯	13.11 ± 0.11	8.8 ± 0.9	8.7 ± 1.0	⋯
		⋯	⋯	⋯	⋯	12.19 ± 0.43	5.4 ± 9.6	−34.0 ± 2.6	⋯

Notes. Best-fit Voigt profile model parameters for Na I systems fit with a single absorbing component are listed in a single table row. For systems fit with two components, we list the total $\log N_{vp}$ of the system in the first row for each sight line and include best-fit $\log N_{vp}$, b_D, and δv values for the individual components in the following two rows.
[a] Upper limits are reported at the 3σ level.
[b] To model this absorber, we fixed the column density to the measured value of N_{aod} as described in Section 4.2.

(This table is available in machine-readable form.)

Straka et al. (2015) are shown in gray. Within our ESI sample, absorption detections span the full range of $R_\perp$ probed, with nondetections arising only within <6 kpc. We note here that several of our foreground galaxies observed at $R_\perp > 6$ kpc may have higher global SFRs ($\gtrsim 10-100\,M_\odot$ yr^{-1}; see Appendix A) than those observed at $R_\perp < 6$ kpc. Under the assumption that galaxies that are more actively star-forming will have larger W_r(Ca II) and W_r(Na I) across a broad range of impact parameters, this potential bias may drive an enhancement in our observed W_r values at large $R_\perp$. While we cannot reliably quantify the global SFRs of our galaxy sample with current data, we can instead draw on the measurements of global M_* described in Section 3 to assess the degree to which an analogous relation between M_* and W_r may impact the distributions of data points shown in Figure 4. The left-hand panel of Figure 2 demonstrates that our sample contains equal numbers of galaxies with stellar masses falling above and below the median value ($\log M_*/M_\odot = 9.3$) at $R_\perp > 6$ kpc. This suggests that the bias described above does not have a major impact on our analysis of the relation between absorber properties and $R_\perp$; however, we caution that new data enabling the measurement of the global SFRs in our foreground galaxies are needed to fully disentangle the relationships between $R_\perp$, global star formation activity, and W_r.

The blue curves in Figure 4 show the power-law relation (with 1σ uncertainties) fit to the mean Ca II K absorption signal measured in SDSS spectra of QSO sight lines versus the projected separation of these QSOs from known foreground systems by Zhu & Ménard (2013). Because this latter analysis included all sight lines having 3 kpc < $R_\perp$ < 10 kpc in a single bin, the fitted relation is insensitive to potential changes in the power-law slope at very small separations. Nevertheless, the absorbers in our data set do not exhibit larger W_r at smaller projected separations as implied by this fit. We caution that the foreground galaxy sample identified by Zhu & Ménard (2013) has higher stellar masses than those we study here (i.e., the median stellar mass in the former sample is $\log M_*/M_\odot \sim 10.3$), which could explain the larger W_r implied by their fitted relation at $R_\perp \sim 3$–4 kpc.

Figure 5 shows the same W_r measurements presented in Figure 4 versus $R_\perp/R_{\rm eff,est}$. We remind the reader that those galaxies probed at $R_\perp/R_{\rm eff,est} > 2$ have systematically lower stellar masses than those probed at $R_\perp/R_{\rm eff,est} < 2$. Moreover, the modeling described in Appendix A suggests the former systems exhibit a broad range of global SFRs, spanning between $\sim 0.5\,M_\odot$ yr^{-1} and $>100\,M_\odot$ yr^{-1}. While absorption nondetections are more evenly distributed across this parameter

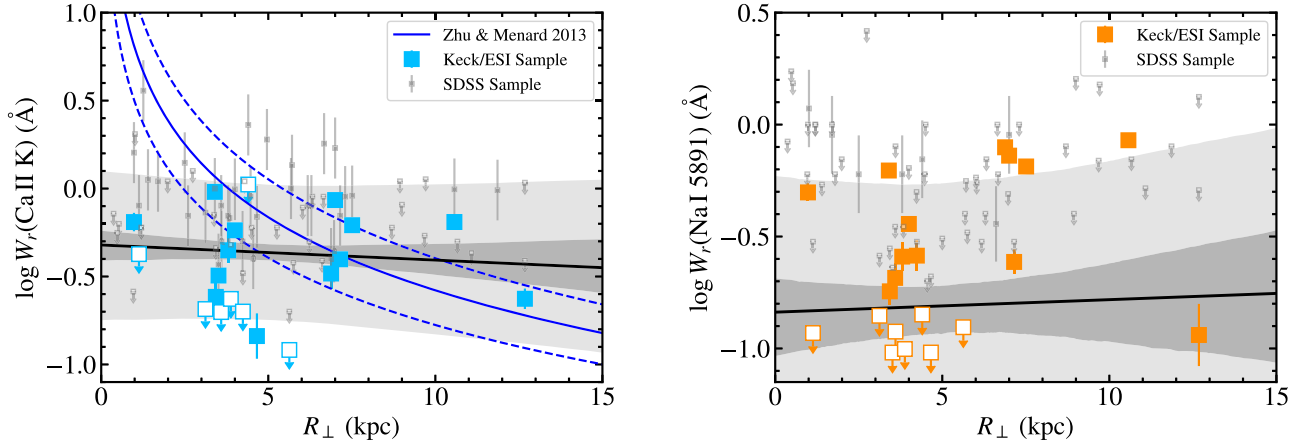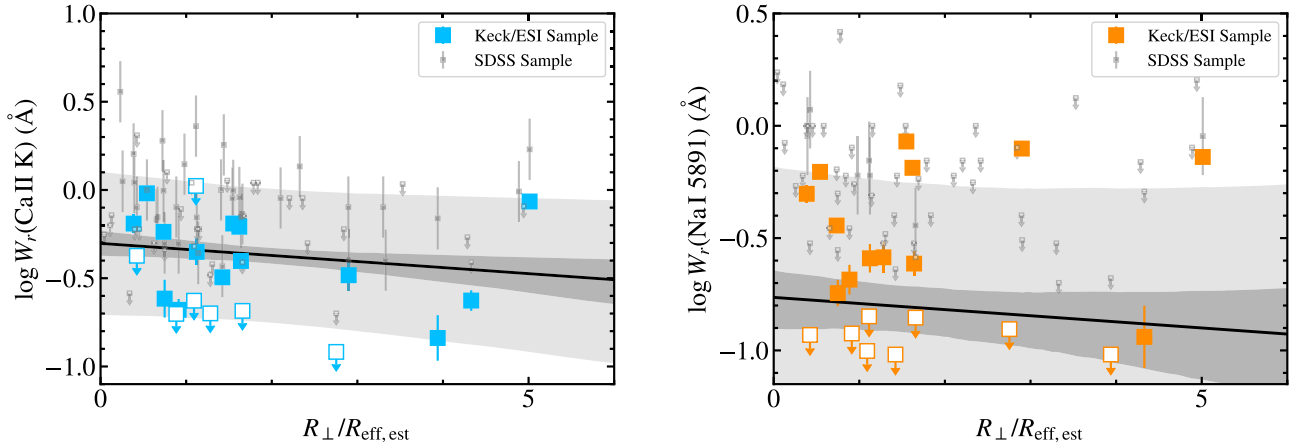**Figure 4.** Total system W_r(Ca II K) (left) and W_r(Na I 5891) (right) versus projected distance from the associated host galaxy. Colored points show constraints from our ESI spectroscopy. Upper limits, indicated with open squares, are shown in cases for which $W_r < 3\,\sigma_{W_r}$ and represent 3σ limits. Gray points show measurements reported in Straka et al. (2015) from their analysis of SDSS spectroscopy probing the parent sample of GOTOQs. We exclude absorbers that were flagged as blended by Straka et al. (2015). We also exclude any systems in which the Ca II K transition falls more than 20 Å blueward of the Lyα emission line of the corresponding QSO to avoid blending from the Lyα forest. Black solid lines show best-fit linear relations between $\log W_r$ and $R_\perp$ (see Section 5.1), and medium gray contours show the inner $\pm34\%$ of the locus of fits drawn at random from the posterior probability density function of each linear model. The light gray region extends the boundaries of the medium gray 1σ region by the best-fit value of σ_C to approximately indicate the degree of intrinsic scatter implied by the data. Our W_r measurements exhibit no apparent anticorrelation with increasing projected distance from the foreground host.

Figure 5. Total system W_r(Ca II K) (left) and W_r(Na I 5891) (right) versus projected distance from the associated host galaxy, normalized by the galaxy's estimated effective radius. Symbols, lines, and contours are as described in the Figure 4 caption. The relation between $\log W_r$(Ca II K) and $R_\perp/R_{\rm eff,est}$ for the combined ESI and SDSS sample has a slope $m = -0.035^{+0.028}_{-0.030}$, indicative of a weak anticorrelation between these quantities. The relation between $\log W_r$(Na I 5891) and $R_\perp/R_{\rm eff,est}$ exhibits no significant anticorrelation.

space than across the range in $R_\perp$, the relation between W_r and $R_\perp/R_{\rm eff,est}$ does not exhibit a clear anticorrelation for either ion.

To quantitatively test for correlations (or a lack thereof) in these quantities, we model these data sets assuming a linear relation between $\log W_r$ and either $R_\perp$ or $R_\perp/R_{\rm eff,est}$:

$$\log\ W_r = b + mR_\perp. \qquad (2)$$

We follow Chen et al. (2010a) and Rubin et al. (2018) to compute the likelihood function for this model. Briefly, for all securely detected W_r values, the contribution to the logarithm of the likelihood is $\chi^2/2$. For nondetections, each term in the product used to compute the likelihood is the integral from $-\infty$ to the value of the W_r upper limit of a Gaussian function similar in form to that used to calculate χ^2 (see Rubin et al. 2018 for the full likelihood function). We also assume that the relation in Equation (2) has an intrinsic cosmic variance, σ_C, such that the Gaussian variance adopted for each measurement in the

likelihood function is $s_i^2 = \sigma_i^2 + \sigma_C^2$, with σ_i equal to the measurement uncertainty in each $\log W_r$ value.

We use the Python software package emcee to perform affine-invariant ensemble Markov Chain Monte Carlo sampling of the posterior probability density function (PPDF) for this model (Foreman-Mackey et al. 2013). We adopt uniform priors for all three parameters within the intervals $-5.0 < m < 5.0$ (with m having units of either kpc^{-1} or being unitless, as appropriate), $-10.0 < b < 10.0$, and $-10.0 < \ln\sigma_C < 10.0$. We implement 100 "walkers," each of which take 5000 steps (the first 1000 of which are discarded) to thoroughly sample the PPDF. We interpret the median and ±34th percentiles of the marginalized PPDF for each parameter as its best value and uncertainty interval.

We show the resulting best-fit relations between $\log W_r$ and either $R_\perp$ or $R_\perp/R_{\rm eff,est}$ for the combined ESI and SDSS data sets in Figures 4 and 5, respectively, with solid black lines. The medium gray contours show the inner $\pm34\%$ of the locus of fits

Table 4
Best-fit Parameters for Linear log $W_r - R_\perp$ Models

Data Set	Relation	m	b	σ_C
ESI & Straka et al. (2015)	log W_r(Ca II K)–$R_\perp$	-0.009 ± 0.015 kpc^{-1}	-0.32 ± 0.09	$0.34^{+0.05}_{-0.04}$
	log W_r(Ca II K)–$R_\perp/R_{\rm eff,est}$	$-0.035^{+0.028}_{-0.030}$	-0.30 ± 0.07	$0.33^{+0.05}_{-0.04}$
	log W_r(Na I 5891)–$R_\perp$	$+0.006^{+0.026}_{-0.027}$ kpc^{-1}	$-0.84^{+0.15}_{-0.18}$	$0.46^{+0.10}_{-0.07}$
	log W_r(Na I 5891)–$R_\perp/R_{\rm eff,est}$	$-0.028^{+0.046}_{-0.053}$	$-0.76^{+0.12}_{-0.14}$	$0.46^{+0.10}_{-0.07}$
ESI Only	log W_r(Ca II K)-$R_\perp$	$+0.022^{+0.031}_{-0.028}$ kpc^{-1}	$-0.64^{+0.17}_{-0.20}$	$0.35^{+0.10}_{-0.07}$
	log W_r(Ca II K)-$R_\perp/R_{\rm eff,est}$	$-0.006^{+0.063}_{-0.061}$	$-0.52^{+0.14}_{-0.15}$	$0.34^{+0.10}_{-0.07}$
	log W_r(Na I 5891)-$R_\perp$	$+0.058^{+0.046}_{-0.042}$ kpc^{-1}	$-1.05^{+0.25}_{-0.30}$	$0.52^{+0.16}_{-0.11}$
	log W_r(Na I 5891)-$R_\perp/R_{\rm eff,est}$	$+0.016^{+0.098}_{-0.097}$	$-0.78^{+0.20}_{-0.23}$	$0.54^{+0.16}_{-0.11}$

for 1000 sets of parameters drawn at random from the PPDF of each data-model comparison. The light gray contours indicate the boundaries of the inner $\pm 34\%$ locus, extended on either side by the best-fit value of σ_C. We also list the best-fit parameters and their uncertainty intervals for each data set in Table 4. Three of the four best-fit values of the slope (m) are consistent with zero, confirming a lack of any significant correlation between both log W_r(Ca II K) and log W_r(Na I 5891) and $R_\perp$, as well as between log W_r(Na I 5891) and $R_\perp/R_{\rm eff,est}$. The log W_r(Ca II K)–$R_\perp/R_{\rm eff,est}$ relation has a slope $m = -0.035^{+0.028}_{-0.030}$, weakly suggestive of an anticorrelation between these variables.

Given our finding in Section 4.2 that the Straka et al. (2015) W_r values are frequently larger than those we measure for the same sight lines, we also perform the same modeling including only our ESI data set. The resulting best-fit model parameters are listed in Table 4. Here again, three of the four best-fit slopes are consistent with zero. Moreover, the log W_r(Na I 5891)-$R_\perp$ relation has a slope that is marginally *positive* ($m = +0.058^{+0.046}_{-0.042}$ kpc^{-1}). All together, we interpret these results as further confirmation of a lack of any anticorrelation between W_r and $R_\perp$ or $R_\perp/R_{\rm eff,est}$.

Keeping in mind the caveat that these findings may be affected by a bias in our galaxy sample toward higher global SFRs at larger $R_\perp$ (as discussed toward the beginning of this section), we note that the lack of a strong dependence of our W_r values on projected distance is unique among the QSO–galaxy pair literature. The vast majority of these studies instead have reported a statistically significant decline in the W_r of a wide range of ionic transitions (including transitions of H I, C II, C III, C IV, Si II, Si III, Mg II, and Ca II) with $R_\perp$ (e.g., Lanzetta & Bowen 1990; Kacprzak et al. 2008; Chen et al. 2010a; Nielsen et al. 2013; Werk et al. 2013; Zhu & Ménard 2013; Burchett et al. 2016; Kulkarni et al. 2022). However, these works have included sight lines over a much larger range of projected separations ($R_\perp \gtrsim 100$ kpc) than are included here, and many of them have included few (if any) sight lines with $R_\perp < 15$ kpc (e.g., Lanzetta & Bowen 1990; Chen et al. 2010a; Werk et al. 2013). The findings of Kacprzak et al. (2013), a study of Mg II absorption along a sample of seven GOTOQ sight lines selected from Noterdaeme et al. (2010) and York et al. (2012), confirm that sight lines with impact parameters $\gtrsim 10$ kpc drive the well-known anticorrelation between W_r(Mg II 2796) and $R_\perp$, while the W_r(Mg II 2796) values for sight lines within this projected distance exhibit no significant dependence on $R_\perp$. On the other hand, Kulkarni et al. (2022) noted that the strong anticorrelation between N(H I) and $R_\perp$ exhibited by their sample of 113 galaxies associated with DLAs and sub-DLAs (assembled from their study of eight GOTOQs and the literature across $0 < z < 4.4$) appears to extend well within $R_\perp < 10$ kpc. This apparent disagreement with both Kacprzak et al. (2013) and the present study may be driven by a variety of factors, including the use of different ionic transitions and quantities characterizing absorption-line strength (i.e., W_r versus N), and differing absorber–galaxy pair selection criteria.

5.2. Column Densities and Covering Fractions

Figure 6 shows the total system column densities (including all velocity components) of Ca II (left) and Na I (right) in each GOTOQ sight line in our sample versus $R_\perp$ (top row) and versus $R_\perp/R_{\rm eff,est}$ (bottom row). As with the W_r values discussed above, the measured column densities do not appear to exhibit any dependence on either $R_\perp$ or $R_\perp/R_{\rm eff,est}$.

We assess the covering fraction (f_C) of these absorbers by dividing the number of systems with column densities above a given threshold by the total number of sight lines (excluding nondetections above the threshold). These thresholds are chosen to lie just above the majority of 3σ upper limits for each ion; i.e., N(Ca II) $> 10^{12.5}$cm^{-2} and N(Na I) $> 10^{12.0}$cm^{-2}. We adopt the ± 34th percentile Wilson score intervals as uncertainty intervals for each covering fraction. Overall, we measure covering fractions f_C (Ca II) $= 0.63^{+0.10}_{-0.11}$ and f_C (Na I) $= 0.57^{+0.10}_{-0.11}$. We also compute covering fractions within two bins in $R_\perp$ and $R_\perp/R_{\rm eff,est}$ and show the results with filled boxes in Figure 6. These covering fractions do not vary significantly (i.e., by $>2\sigma$) as a function of either of these measures of projected distance.

It is notable that the overall f_C values for Ca II and Na I are statistically consistent with each other, given that Ca II is known to trace a wider range of gas densities and temperatures (Phillips et al. 1984; Vallerga et al. 1993; Ben Bekhti et al. 2012; Murga et al. 2015). If we instead adopt equivalent column density thresholds for both ions ($N > 10^{12.5}$ cm^{-2}), we find a value f_C (Na I) $= 0.33^{+0.11}_{-0.09}$, which is 1.9σ below that of f_C(Ca II). This difference accords with a picture in which Na I-absorbing structures are smaller in size and/or less abundant than Ca II-absorbing clouds (e.g., Bish et al. 2019). These values are also broadly consistent with the incidence of intermediate and high-velocity Ca II and Na I absorbers detected toward a sample of 408 QSO sight lines probing the Milky Way disk–halo interface and halo by Ben Bekhti et al. (2012), in spite of their use of more sensitive column density thresholds: these authors measured $f_C = 0.5$ for a threshold N(Ca II) $\geqslant 10^{11.4}$cm^{-2} and $f_C = 0.35$ for a threshold N(Na I) $\geqslant 10^{10.9}$cm^{-2}. Similar covering fractions for these ions were measured toward multiple stellar sight lines probing intermediate-velocity material ~ 3 kpc above the Milky Way's disk by Bish et al. (2019; i.e., f_C (log N (Ca II) $>$ 11.5) $= 0.63^{+0.07}_{-0.14}$ and f_C (log N (Na I) > 11.3) $= 0.26^{+0.06}_{-0.08}$).
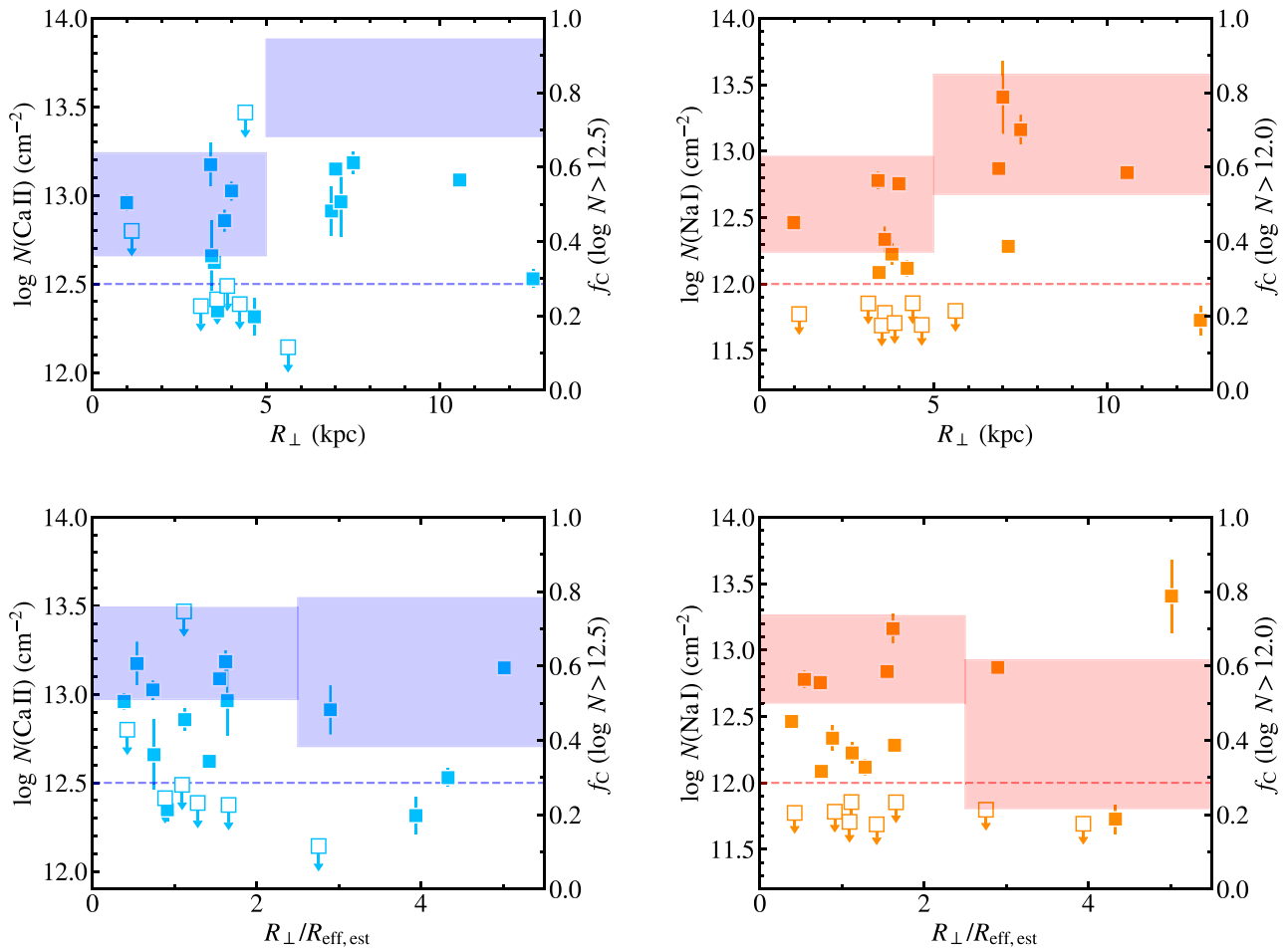
Figure 6. Top row: total system column density of Ca II (left) and Na I (right) versus projected distance from the associated GOTOQs. Open squares with downward arrows represent 3σ upper limits calculated using the apparent optical depth method. The filled boxes indicate the ±34th percentile Wilson score confidence intervals, with respect to the right axes, for the covering fraction of absorbers having log N(Ca II) > 12.5 and log N(Na I) > 12.0, respectively. Bottom row: same as above, vs. $R_\perp/R_{\rm eff,est}$.

This implies that our GOTOQ sight lines have overall higher column densities than those measured in both the Ben Bekhti et al. (2012) and Bish et al. (2019) samples.

We speculate that this may be due to the limited path through the Milky Way probed by the stellar and QSO sight lines used in these studies. In particular, because the focus of these works is on characterizing extraplanar material, they have explicitly excluded absorbers having velocities consistent with that of the Milky Way's disk rotation curve (i.e., ISM absorbers) from their analyses. The intermediate- and high-velocity clouds targeted by Ben Bekhti et al. (2012) are typically found to be located within <2.5 kpc and ~5–20 kpc away from the Milky Way's disk, respectively, in cases in which distance information is available (see Richter 2017 and references therein). Our GOTOQ sight lines, by contrast, are sensitive to all absorbers above our column density detection threshold (log N(Ca II) $\gtrsim$ 12.1–12.4 and log N(Na I) $\gtrsim$ 11.9) regardless of velocity or location along the line of sight. This bias is compounded by a lack of Milky Way halo sight lines located at low Galactic latitudes: existing sight line samples probe relatively short paths through the disk and extraplanar region due to their height above the disk plane (e.g., Bish et al. 2021).

Finally, we note that our Ca II and Na I covering fractions are significantly lower than the unity covering fraction measured for Mg II absorbers having W_r(Mg II 2796) > 1 Å detected along the

seven GOTOQ sight lines studied by Kacprzak et al. (2013). These absorbers have larger W_r values than any in our sample and probe a broader range of gas phases that are known to extend well beyond galactic disks into their halos (e.g., Bergeron & Stasińska 1986; Chen et al. 2010a; Nielsen et al. 2013; Lan et al. 2014).

Figure 7 compares our total column density constraints for Na I and Ca II in individual sight lines. We find that, in general, larger column densities of Na I are associated with larger column densities of Ca II. The purple filled region in this figure indicates the range in the average ratio $\langle N({\rm Na\,I})/N({\rm Ca\,II})\rangle \approx 0.2$–0.9 measured along high-latitude Milky Way halo sight lines by Murga et al. (2015). This latter work analyzed the coadded spectra of many thousands of extragalactic sources, and the absorption signal they report arises from material at all velocities along the line of sight (including contributions from both the Milky Way's ISM and CGM). Our measurements largely fall within this range, suggesting that the gaseous environments probed by our QSO sample are similar to those arising in the Milky Way.

5.3. Absorption Kinematics

The best-fit component velocities (relative to $z_{\rm H\alpha}$) of each absorption system with a total $W_r > 3\sigma_{W_r}$ are shown in Figure 8 vs. projected distance from the associated galaxy host. The
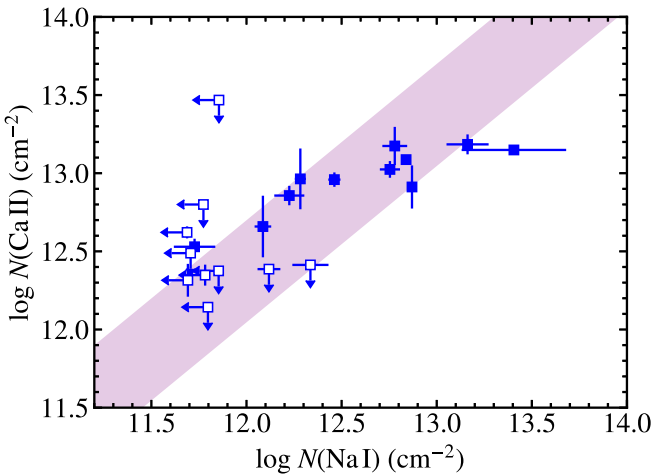
Figure 7. Total system column density of Ca II versus that of Na I in individual GOTOQ sight lines. Sight lines along which we do not securely detect one or both of these ions are indicated with open squares placed at the corresponding 3σ upper limit. The purple filled region indicates the range in the average ratio N(Na I)/N(Ca II) observed toward high Galactic latitude sight lines probing the Milky Way by Murga et al. (2015).

uncertainty interval on each point is set to extend from $\delta v_{90,\ \text{left}}$ to $\delta v_{90,\ \text{right}}$ to indicate the velocity space covered by each system. We remind the reader that $z_{\text{H}\alpha}$ need not be equivalent to the average redshift of each host galaxy but rather indicates the redshift of nebular emission along the same sight line as that used to probe the absorbing gas. We therefore interpret absorption with velocities very close ($|\delta v| \lesssim 10\,\text{km s}^{-1}$) to $z_{\text{H}\alpha}$ as interstellar material lying in the host galaxy's disk and rotating with its H II regions. We assume that absorbers with larger velocity offsets (or extents) may be extraplanar in nature and/or part of ongoing bulk outflow from or inflow toward the disk. This rough velocity criterion is motivated by the theoretical considerations laid out in Section 6, where they will be further refined (to account for the M_* and $R_\perp$ of each system, as well as uncertainties in foreground galaxy orientation). For comparison, the detailed study of the spatially resolved velocity distributions of disk and extraplanar absorbers in the nearby galaxy M33 by Zheng et al. (2017) identified Si IV components having velocities within $\pm 20\,\text{km s}^{-1}$ of the local H I 21 cm emission peak as "disk" absorbers, and uncovered numerous extraplanar absorbers at relative velocities $\pm 30-110\,\text{km s}^{-1}$.

Among the 20 Ca II velocity components included in Figure 8, only three (15%) have $|\delta v| > 50\,\text{km s}^{-1}$; 11 (55%) have $|\delta v| > 20\,\text{km s}^{-1}$; and 14 (70%) have $|\delta v| > 10\,\text{km s}^{-1}$. The remaining six systems have velocity centroids consistent with galactic disk rotation. The Δv_{90} values for the Ca II absorbers, however, lie in the range $50\,\text{km s}^{-1} \leqslant \Delta v_{90} \leqslant 180\,\text{km s}^{-1}$, and thus imply the presence of outflowing/inflowing absorbing material in every case. The Na I absorbers exhibit component velocity offsets at yet lower rates: among the 17 components shown, only one (6%) has $|\delta v| > 50\,\text{km s}^{-1}$, six (35%) have $|\delta v| > 20\,\text{km s}^{-1}$, and only eight (47%) have $|\delta v| > 10\,\text{km s}^{-1}$. These profiles are all likewise kinematically broad ($50\,\text{km s}^{-1} \leqslant \Delta v_{90}(\text{Na I }5891) \leqslant 150\,\text{km s}^{-1}$), suggesting that the ongoing fountain motions traced by Ca II also include a cold component.

For reference, Figure 8 shows the radial velocity that would be required to escape a dark matter halo having $M_h = 10^{10} M_\odot$, assuming that $R_\perp$ is equal to the total distance (R) from the halo

center (rather than the projected distance), and that $v_{\text{esc}} = \sqrt{2GM_h/R}$. Our foreground systems have a range in stellar mass $7.4 \lesssim \log M_*/M_\odot \lesssim 10.6$, implying they range in halo mass over $10.3 \lesssim \log M_h/M_\odot \lesssim 12.0$ (Moster et al. 2013); thus, the escape velocity of an $M_h = 10^{10} M_\odot$ halo may safely be considered the minimum required for these absorbers to escape from any system in our sample. With the caveat that our spectroscopy is sensitive only to motion along the line of sight (such that our δv values are likely somewhat lower than the three-dimensional velocity of the gas), we find that none of the absorbers in our sample have central velocities close to that required for escape from their host systems. Moreover, none of the velocity limits of the profiles (indicated by the [$\delta v_{90,\ \text{left}}$, $\delta v_{90,\ \text{right}}$] intervals) extend beyond this escape velocity limit.

The rightmost panel of Figure 8 shows the distribution of the best-fit b_D values for our Ca II and Na I absorption component sample. The median value of the former is $18.5\,\text{km s}^{-1}$, while the median value of $b_D(\text{Na I})$ is $10.5\,\text{km s}^{-1}$, close to the resolution of our spectrograph. In contrast, the QSO absorption-line study of Ca II and Na I absorption in Milky Way disk–halo clouds by Ben Bekhti et al. (2012) measured median Doppler parameter values of $3.3\,\text{km s}^{-1}$ for Ca II and $2.1\,\text{km s}^{-1}$ for Na I, with maximum values of $\approx 10\,\text{km s}^{-1}$ for both ions. This suggests that the absorbing components in our sample are likely composed of multiple individual "clouds," and that our b_D values are predominantly reflective of turbulent velocity dispersions among these clouds (with a subdominant contribution from thermal broadening).

Figure 9 shows the best-fit δv value for each Ca II component versus the corresponding value of $\delta v(\text{Na I})$ for each system. Systems for which we have fit Ca II (or Na I) with a single component and the other ion with two components appear twice, each with the same y-axis (or x-axis) value. There are three systems for which we fit two velocity components to both ions; in these cases, we match components in order of increasing velocity. We do not require that the δv values for Ca II and Na I fall within some minimum velocity offset to include them here; instead, we use this figure to assess the degree to which our fitted Na I and Ca II components exhibit similar velocities. The component velocities align closely along many of our sight lines: the quantity $|\delta v(\text{Ca II}) - \delta v(\text{Na I})|$ has a median value $10.9\,\text{km s}^{-1}$, and exceeds $25\,\text{km s}^{-1}$ for only four of the 17 component pairs considered. However, the Pearson correlation coefficient for these measurements is 0.23 with a p-value of 37%, indicating a relatively high likelihood that uncorrelated data could yield a similar or more extreme coefficient. If we consider only those systems for which we adopt consistent numbers of components for both Ca II and Na I, we measure a Pearson correlation coefficient of 0.35 with a -value of 29%.

Given that our spectroscopy likely cannot resolve the individual absorbing structures producing the observed line profiles, as well as the significant probability that Na I occurs in fewer of these structures than does Ca II (e.g., Ben Bekhti et al. 2012; Bish et al. 2019), our simple approach to modeling these profiles likely obfuscates the velocity alignment of these ions. Even with this limitation, our data set points to a relatively high degree of velocity coherence between the two gas phases we trace. In Milky Way studies, the kinematics of these ions are typically compared via analysis of the $N(\text{Ca II})/N(\text{Na I})$ ratio as a function of velocity relative to the local standard of rest (LSR; e.g., Routly & Spitzer 1952; Sembach & Danks 1994; Ben Bekhti et al. 2012). This ratio has average values of $N(\text{Ca II})/N$
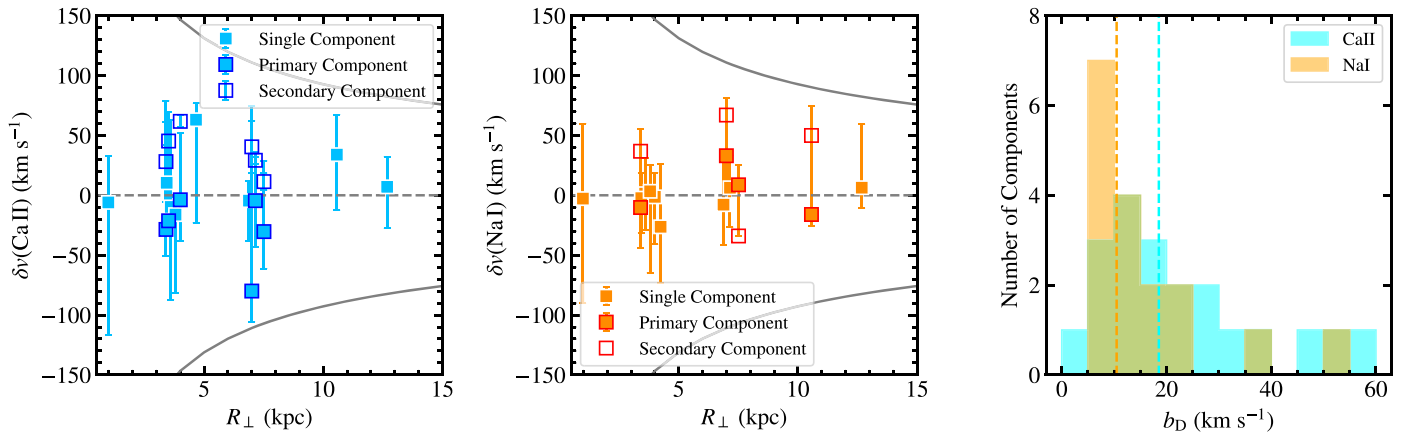
Figure 8. Absorption velocity offsets relative to $z_{H\alpha}$ for Ca II (left) and Na I (middle) for each securely detected absorption system versus projected distance from the galaxy host. Systems fit with single velocity components are shown with solid light blue and orange squares. The primary and secondary components of systems fit with two velocity components are shown with light blue/orange squares outlined with dark blue/red and open squares outlined with dark blue/red, respectively. Error bars show the span of velocities included in the Δv_{90} measurement for the Ca II K and Na I 5891 lines. The gray curves indicate the radial velocity required to escape an $M_h = 10^{10} M_\odot$ halo (a conservative minimum escape velocity given the stellar mass distribution of our sample) as a function of total distance from the halo center. The projected velocity of all detected absorption is well below this threshold. The rightmost panel shows the distribution of best-fit b_D values for all components in our Ca II (cyan) and Na I (orange) absorbers. The median value of each distribution is shown with a vertical dashed line.

(Na I) ≈ 0.69 at velocities close to the LSR and increases at larger velocity offsets (likely due to the so-called Routly-Spitzer effect; Routly & Spitzer 1952; Sembach & Danks 1994). While these measurements are not directly analogous to those presented in Figure 9, they are similarly suggestive of kinematic coherence of these ions.

5.4. Relation between W_r and Dust Reddening

Na I and Ca II absorption is known to be correlated with dust across a variety of astrophysical environments, including in the Milky Way ISM and halo (e.g., Sembach et al. 1993; Munari & Zwitter 1997; Poznanski et al. 2012; Murga et al. 2015) and in external galaxies (e.g., Wild & Hewett 2005; Chen et al. 2010b; Phillips et al. 2013; Baron et al. 2016; Rupke et al. 2021). However, current evidence suggests that the strength and form of the relationship between $E(B - V)$ and W_r(Na I) in particular depends on the environment probed and/or on the approach to measuring these quantities (e.g., Rupke et al. 2021). Here we investigate the relationship between dust reddening and W_r(Na I) and W_r(Ca II) in our GOTOQ sample, and compare it to that derived for the Milky Way.

We adopt the estimate of $E(B - V)_{(g-i)}$ reported by Straka et al. (2015) for the QSOs in our sample as a proxy for the dust column density associated with each foreground host. These estimates are based on the observed-frame $(g - i)$ color excess of each QSO relative to the median $(g - i)$ for QSOs at the same redshift in the fourth edition of the SDSS Quasar Catalog (Schneider et al. 2007). In a study of the relation between QSO colors and the presence and strength of foreground Mg II absorbers in the SDSS QSO sample, York et al. (2006) found that the QSO color excess $\Delta(g - i)$ is tightly correlated with the dust reddening $E(B - V)$ associated with foreground absorbers and measured from composite QSO spectra shifted into the absorber rest frame. These authors adopted an SMC reddening law (Prevot et al. 1984) to calculate the expected relation $E(B - V)_{(g-i)} = \Delta(g - i)(1 + z_{abs})^{-1.2}/1.506$, and found that the average $E(B - V)_{(g-i)}$ in samples of $\gtrsim 100$ objects corresponds closely to the $E(B - V)$ of their composite spectra: $\langle E(B - V)_{(g-i)} \rangle = 0.98 \times E(B - V) - 0.002$. However, York et al. (2006) also demonstrated that $\Delta(g - i)$ values for
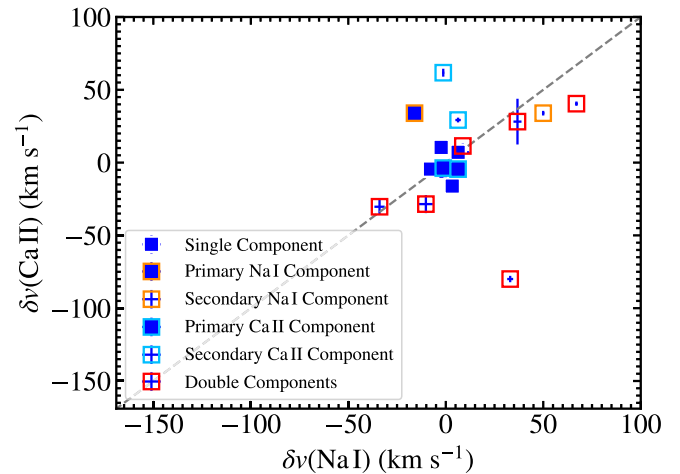
Figure 9. Fitted absorption velocity offsets relative to $z_{H\alpha}$ for securely detected Ca II systems versus those for securely detected Na I systems. Error bars show the uncertainties in these fitted values. Absorbers fit with single velocity components in both transitions are shown with solid blue squares. Absorbers in which Ca II was fit with one component and Na I was fit with two components are indicated with solid blue and open squares outlined in orange. Absorbers in which Na I was fit with one component and Ca II was fit with two components are indicated in a similar fashion, as listed in the legend. Velocities for absorbers in which both ions were fit with two components are shown with open red squares.

individual quasars with no detected foreground absorbers exhibit significant scatter with FWHM ≈ 0.27 mag[17] (with a mean value $\Delta(g - i) = -0.013$). This implies an intrinsic dispersion $\sigma_{intr}(\Delta(g - i)) = 0.12$.

To estimate the total uncertainty in each $E(B - V)_{(g-i)}$ value, we consider both this intrinsic scatter and uncertainty due to measurement error. Straka et al. (2015) stated that the maximum error in their measurements of apparent magnitudes for both the QSOs and foreground galaxies in their GOTOQ sample is 0.05 mag. We therefore assume a measurement error of $\sigma_{meas}(\Delta(g - i)) = 0.07$. We multiply both σ_{meas} and σ_{intr} by

---

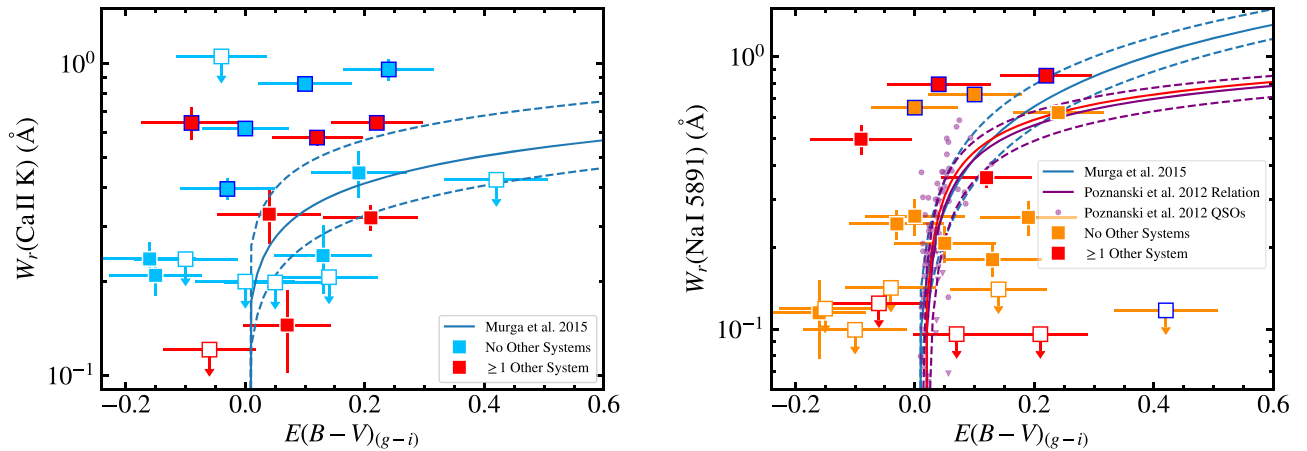[17] This quantity is estimated by fitting a Gaussian model to a digitized version of the data in Figure 3 of York et al. (2006).

Figure 10. Total system W_r(Ca II K) (left) and W_r(Na I 5891) (right) versus the dust reddening measured along the QSO sight line, $E(B-V)_{(g-i)}$. Upper limits, indicated with open squares, are shown in cases in which $W_r < 3\sigma_{W_r}$, and represent 3σ limits. Sight lines shown in light blue and orange have no intervening systems that are unassociated with the known foreground galaxy. Sight lines indicated in red exhibit one or more unassociated intervening systems in their SDSS spectra. The solid blue curves show the best-fit relations between the W_r of these ions due to the Milky Way's ISM/halo and dust reddening measured by Murga et al. (2015). The dashed blue curves represent the $\pm 1\sigma$ uncertainty in these fits. The purple curves show the best-fit relation (and the $\pm 1\sigma$ uncertainty in the relation) between W_r(Na I 5891) and dust reddening in the Milky Way measured by Poznanski et al. (2012). The small purple circles/triangles show W_r(Na I 5891) values/3σ upper limits measured from high-resolution QSO spectra by Poznanski et al. (2012), plotted versus the reddening toward that coordinate in the Planck Collaboration et al. (2016) dust map. Data points outlined in dark blue are offset by $>3\sigma$ from the closest point on the best-fit Murga et al. (2015; left) and Poznanski et al. (2012; right) relations.

the quantity $(1 + z_{abs})^{-1.2}/1.506$ and add the results in quadrature to compute a total $\sigma_{tot}(E(B-V)_{(g-i)})$ for each GOTOQ sight line.

Figure 10 shows $E(B-V)_{(g-i)}$ estimates for our sample with error bars indicating $\sigma_{tot}(E(B-V)_{(g-i)})$ versus the total W_r of Ca II K and Na I 5891 for each system. Light blue and orange points indicate sight lines lacking any intervening absorbers (other than the system associated with $z_{H\alpha}$). Red points indicate sight lines along which between one and nine unassociated intervening absorbers were detected in their SDSS spectra by Straka et al. (2015). These seven QSOs may be subject to some additional reddening from these intervening absorbers, although Straka et al. (2015) found that dust in the GOTOQs themselves is likely the dominant source of attenuation for these systems.

We first note that there is no relationship between $E(B-V)_{(g-i)}$ and either W_r(Ca II K) or W_r(Na I 5891) evident among our GOTOQ sample. The distribution of W_r values in subsamples having $E(B-V)_{(g-i)} < 0.05$ and $E(B-V)_{(g-i)} > 0.05$ have medians of W_r(Ca II K) = 0.28 Å and 0.38 Å, respectively, with dispersions of 0.18–0.31 Å, and medians of W_r(Na I 5891) = 0.18 Å and 0.22 Å, with dispersions of 0.29–0.31 Å (adopting the measured values of W_r for all sight lines, rather than upper limits for nondetections). We therefore are not sensitive to any significant shift in these distributions between low and high reddening values.

We also assess the degree to which our data set is consistent with the average relationships between dust reddening and Ca II/ Na I absorption strength in the Milky Way. These relationships have been investigated both in works using high-resolution spectroscopy of samples of <100 QSOs or early-type stars (e.g., Richmond et al. 1994; Munari & Zwitter 1997), and more recently in studies taking advantage of the >100,000 QSO spectra and >800,000 galaxy spectra obtained over the course of the SDSS (Abazajian et al. 2009). These latter works (Poznanski et al. 2012; Murga et al. 2015) grouped these spectra into bins based on the dust reddening of each source implied by the Schlegel et al. (1998) map of the dust distribution across the sky. They then constructed the median stack of the spectra in each bin and

measured the W_r of Ca II H & K (in the case of Murga et al. 2015) and the W_r for both Na I doublet transitions in each stack. The best-fit relations between $E(B-V)$ and W_r of the relevant transition reported in these studies are included as solid curves in Figure 10. Dashed curves show the same relations with the best-fit parameters offset by their $\pm 1\sigma$ uncertainties. Also included in the right-hand panel of Figure 10 are W_r(Na I) measurements reported by Poznanski et al. (2012) for a small sample of high-resolution QSO spectra. We estimate the reddening of these sources by querying the Planck Collaboration et al. (2016) dust map available with the dustmaps Python package (Green 2018).

Most of the measurements for our GOTOQ sample are formally consistent with these relationships, given the large uncertainties in our $E(B-V)_{(g-i)}$ estimates. However, their distribution appears to exhibit significant scatter around these relationships, and indeed more dispersion than the Poznanski et al. (2012) sample of individual W_r(Na I) measurements. To quantitatively identify outliers in our sample, we first determine the closest point on each best-fit relation (x_j, y_j) to that of each data point (i.e., such that the Euclidean distance $d_j = \sqrt{(E(B-V)_{(g-i),j} - x_j)^2 + (W_{r,j} - y_j)^2}$ is minimized). For sight lines that did not yield significant detections of a given ion, we use the formally measured value of W_r (rather than its upper limit) to compute d_j. We then determine the significance of the distance d_j by computing

$$\mathcal{N}(\sigma_{d,j}) = \sqrt{\left(\frac{E(B-V)_{(g-i),j} - x_j}{\sigma_{tot}(E(B-V)_{(g-i),j})}\right)^2 + \left(\frac{W_{r,j} - y_j}{\sigma_{W_{r,j}}}\right)^2}.$$

The seven systems for which $\mathcal{N}(\sigma_{d,j}) > 3$ relative to the best-fit Murga et al. (2015) relation for Ca II are outlined in dark blue in Figure 10 (left). All of these systems lie at W_r values $\approx$0.2–0.5 Å higher than that implied by the QSO's dust reddening level. We outline in dark blue the five Na I systems for which $\mathcal{N}(\sigma_{d,j}) > 3$ relative to the best-fit Poznanski et al. (2012) relation in the right panel of Figure 10. Again, most of these systems have higher W_r(Na I 5891) values than would be predicted by Poznanski et al. (2012). The overall high incidence of these outliers (comprising 33% and 24% of our Ca II and Na I samples, respectively), implies
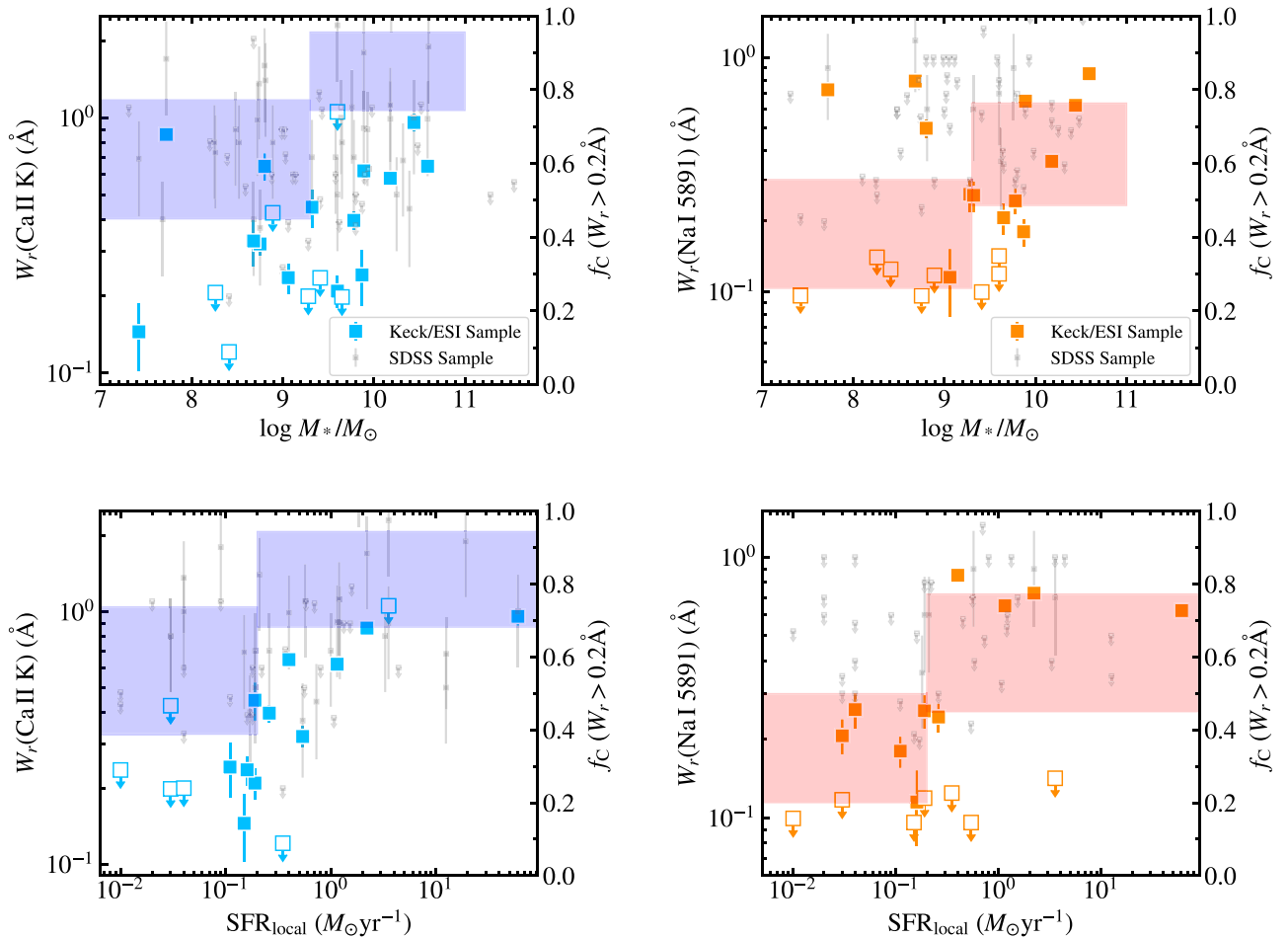
Figure 11. Total system $W_r(\text{Ca II K})$ (left) and $W_r(\text{Na I } 5891)$ (right) versus $\log M_*/M_\odot$ (top row) and SFR$_{\text{local}}$ (bottom row) measured for the foreground host system. Large colored points indicate constraints from our ESI spectroscopy. Upper limits, indicated with open squares, are shown in cases in which $W_r < 3\sigma_{W_r}$ and represent 3σ limits. Gray points show measurements reported in Straka et al. (2015) for the parent GOTOQ sample. The filled boxes indicate the ± 34th percentile Wilson score confidence intervals, with respect to the right axes, for the covering fraction of absorbers having $W_r > 0.2$ Å in our ESI sample.

that these best-fit relations may underpredict the amount of low-ion metal absorption associated with low values of $E(B-V)$. If we apply a 14% recalibration to the $E(B-V)$ values used in Poznanski et al. (2012) and Murga et al. (2015) as recommended by Schlafly & Finkbeiner (2011), the number of Na I outliers remains the same, and the number of Ca II outliers is reduced to six (or 29% of our sample).

Studies of dust across a range of environments, from the SMC (Welty et al. 2006, 2012) to the ISM of QSO host galaxies (Baron et al. 2016), have likewise indicated that $E(B-V)$ values of $\gtrsim 0.05$ mag are associated with higher $W_r(\text{Na I})$ than implied by Poznanski et al. (2012). As the Poznanski et al. (2012) relation is commonly invoked to estimate the reddening of both type I and II supernovae in combination with measurements of $W_r(\text{Na I})$ in spectroscopy of these objects (e.g., Smith & Andrews 2020; Bruch et al. 2021; Dastidar et al. 2021), it is important to appreciate potential biases that may arise from this calibration (e.g., Phillips et al. 2013). Moreover, given the wide range in stellar masses of our GOTOQ host galaxies, we suggest that our sample may better represent the varied dust and ISM properties of supernova host galaxies than those focused purely on the Milky Way, SMC, or QSO host systems.

5.5. Relations between Absorption Strength and Host Galaxy Properties

Here we investigate the relationships between the W_r of Ca II and Na I absorption and the stellar masses and local star formation activity of the associated foreground host galaxies. Figure 11 shows our total system $W_r(\text{Ca II K})$ and $W_r(\text{Na I } 5891)$ measurements versus $\log M_*/M_\odot$ (top row) and SFR$_{\text{local}}$ (bottom row). Our $W_r(\text{Ca II K})$ values appear to exhibit correlations with both SFR$_{\text{local}}$ and M_*. The Pearson correlation coefficient for the relationship between our directly measured $W_r(\text{Ca II K})$ values and foreground galaxy local SFR is $\rho_P = 0.61$ with a p-value $= 0.009$, indicative of a relation that is close to linear and a very low probability that these variables are uncorrelated. If we exclude the system with the highest-SFR$_{\text{local}}$ value (of $60.3\ M_\odot\ \text{yr}^{-1}$) from this analysis, we find a $\rho_P = 0.50$ with a p-value $= 0.05$, confirming that this correlation is not driven solely by a single extreme system. For the relationship between $W_r(\text{Ca II K})$ and $\log M_*/M_\odot$, we find $\rho_P = 0.35$ with $p = 0.12$, which does not rule out the null hypothesis that these variables are uncorrelated. Our $W_r(\text{Na I } 5891)$ measurements, shown in the right panels of Figure 11, yield correlation coefficients of $\rho_P = 0.35$ and 0.27 when considered versus SFR$_{\text{local}}$ and $\log M_*/M_\odot$, respectively, with

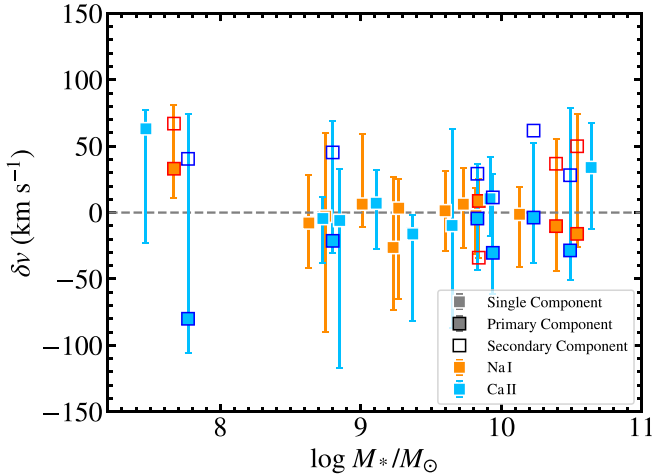**Figure 12.** Fitted component velocity offsets relative to $z_{H\alpha}$ for Ca II (light blue) and Na I (orange) absorbers. Systems fit with single velocity components are shown with solid light blue and orange squares. The primary and secondary components of systems fit with two components are shown with filled and open squares outlined in a complementary color. Error bars show the span of velocities included in the Δv_{90} measurement for the Ca II K and Na I 5891 lines. Symbols have been offset horizontally by ± 0.1 for clarity.

associated p-values in the range $0.17 \leqslant p \leqslant 0.24$. These values likewise do not rule out a lack of correlation between these quantities.

We also assess the covering fraction of strong Ca II and Na I absorbers as a function of SFR_{local} and M_*. Here, we consider strong systems to have $W_r > 0.2$ Å and divide our sample into bins at the median values $\log M_*/M_\odot = 9.3$ and $SFR_{local} = 0.2 M_\odot \, yr^{-1}$. We calculate the incidence and corresponding uncertainty intervals of strong absorbers in each bin as described in Section 5.2 and show the results with filled boxes in Figure 11. Our f_C estimates do not differ significantly at low versus high SFR_{local} or stellar mass. Instead, we find that even systems having $\log M_*/M_\odot < 9.3$ have $f_C(W_r(Ca \, II \, K) > 0.2 \, \text{Å}) = 0.63^{+0.14}_{-0.18}$ and $f_C(W_r(Na \, I \, 5891) > 0.2 \, \text{Å}) = 0.40^{+0.16}_{-0.14}$. We measure similar covering fractions for systems with $SFR_{local} < 0.2 M_\odot \, yr^{-1}$: $f_C(W_r(Ca \, II \, K) > 0.2\text{Å}) = 0.57^{+0.17}_{-0.18}$ and $f_C(W_r(Na \, I \, 5891) > 0.2 \, \text{Å}) = 0.33^{+0.17}_{-0.13}$. These fractions suggest that both transitions may be utilized to trace ISM kinematics in down-the-barrel spectroscopy across the galaxy population, including in systems with $\log M_*/M_\odot \lesssim 9.0$ (e.g., Schwartz & Martin 2004).

Finally, we investigate the relationship between our δv measurements for individual absorption components (presented in Section 5.3) and both $\log M_*/M_\odot$ and SFR_{local}. We show the former in Figure 12. While we do not uncover notable trends in either of these relations, this figure highlights the relatively high-velocity offsets ($\delta v \sim 33-80 \, km \, s^{-1}$) of all primary and secondary components detected close to the two lowest-M_* foreground systems in our sample (having $\log M_*/M_\odot < 8$). Among the 27 single/primary component velocities shown, only one other system has a primary component velocity offset $>33 \, km \, s^{-1}$. Because such large δv values are unusual at $\log M_*/M_\odot > 8.5$, and given the high equivalent widths of the absorption associated with one of these sight lines (GOTOQJ1238+6448 has $W_r(Ca \, II \, K) = 0.86 \pm 0.04$ Å and $W_r(Na \, I \, 5891) = 0.73 \pm 0.03$ Å), we speculate that these absorbers may in fact be associated with other nearby systems that failed to give rise to line emission

that could be detected in the SDSS or ESI spectra. Alternatively, this absorption may be tracing either outflowing material or ongoing accretion.

Regardless of whether we exclude these very low-M_* systems from our sample, we measure a statistically significant correlation between the local SF activity in our foreground galaxies and $W_r(Ca \, II \, K)$ (i.e., the subsample having $\log M_*/M_\odot > 8$ yields $\rho_P = 0.72$ and $p = 0.002$). This finding is reminiscent of the positive correlation between $H\alpha$ flux and $W_r(Ca \, II \, K)$ identified among the GOTOQ parent sample by Straka et al. (2015) and is suggestive of a physical link between star formation activity and the strength/velocity spread of Ca II absorption in the ISM and halo. We discuss the implications of this finding in Section 7.2.

6. A Simple Model of the ISM Contribution to GOTOQ Ca II and Na I Column Densities and Kinematics

Our QSO sight line sample is unusual in the context of CGM studies for its close impact parameters (over the range $R_\perp = 1-13$ kpc). A minority of these sight lines lie within the estimated half-light radius of the foreground host, and, as a consequence of our selection technique, all of our sample sight lines lie within the extent of emission from H II regions and/or an ionized gas layer. Moreover, it is well known that the H I component of disk galaxies is greater in radial extent than that of the stellar or ionized gas component (e.g., the ratio $R_{HI}/R_{25} \gtrsim 1.5-2$; Broeils & Rhee 1997; Swaters et al. 2002; Begum et al. 2008; Wang et al. 2013, 2016). Each of our GOTOQ sight lines is therefore very likely to be probing the warm and/or cold neutral medium within this disk, along with any outflowing or infalling material along the line of sight. Here we consider the extent to which (1) the column densities we measure are consistent with those of a neutral gas disk having a Ca II and Na I distribution similar to that observed in the Milky Way; and (2) the kinematics of our absorber sample are consistent with those predicted for the ISM of galaxies with similar stellar masses.

6.1. Column Densities

It is common in the literature to describe the interstellar density distribution of a given ion as an exponential function that decreases with height $|z|$ above the Milky Way disk plane: $n(z) = n_0 e^{-|z|/h}$ (e.g., Bohlin et al. 1978; Jenkins 1978; Edgar & Savage 1989; Sembach & Danks 1994; Savage et al. 2003; Savage & Wakker 2009). The scale height, h, and the mid-plane density, n_0, may then be constrained by fitting this function to observations of ionic column densities toward samples of Milky Way disk and halo stars (and/or quasars). Sembach et al. (1993) and Sembach & Danks (1994) carried out such a study focusing on Ca II and Na I, finding $n_0(Ca \, II) = 6.85^{+0.76}_{-0.41} \times 10^{-10} \, cm^{-3}$, $h(Ca \, II) = 0.82^{+0.07}_{-0.09}$ kpc, $n_0(Na \, I) = 1.27^{+0.20}_{-0.18} \times 10^{-9} \, cm^{-3}$, and $h(Na \, I) = 0.43^{+0.12}_{-0.08}$ kpc. We adopt these values to build our ISM model. We further assume that the disk density declines exponentially with radius, with the scale radius measured from 21 cm mapping of the Milky Way H I distribution ($R_S = 3.75$ kpc; Kalberla & Kerp 2009). We may therefore write our adopted disk density distribution as

$$n(r, z) = n_0 \exp\left[-\frac{r}{R_S} - \frac{|z|}{h} \right]. \quad (3)$$

Given this density distribution, the total column density observed along a quasar sight line passing through the disk oriented at an inclination i at a location (x, y) may be calculated via the integral
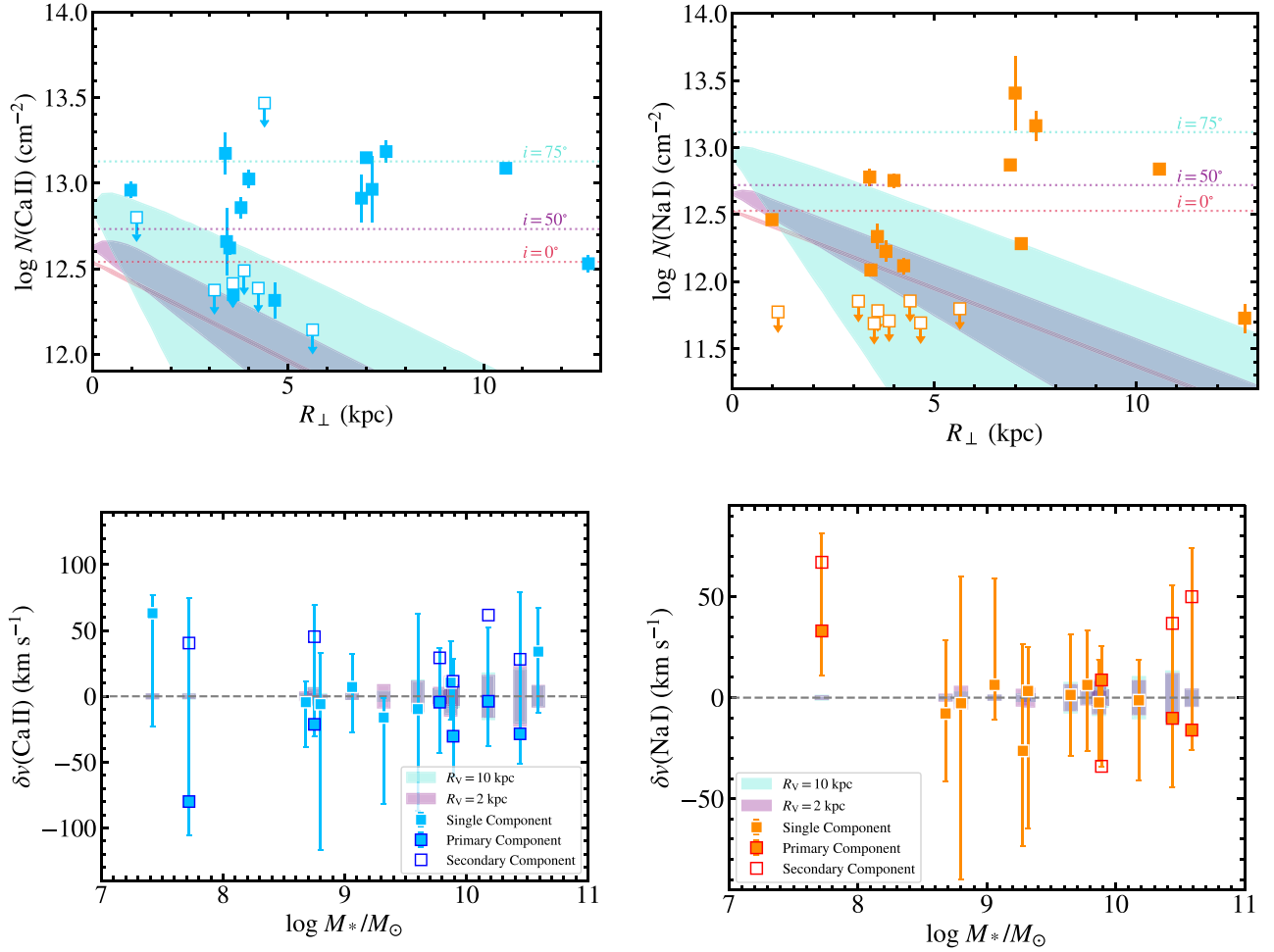
Figure 13. Top row: total system column density of Ca II (left) and Na I (right) versus projected distance from the associated GOTOQs. Symbols correspond to those used in Figure 6. The filled regions indicate the range in column densities predicted for a Milky Way–like ISM observed from an external viewpoint using the simple model described in Section 6.1, and assuming three different disk inclinations ($i = 0°$, $50°$, and $75°$, shown in red, purple, and turquoise, respectively). The horizontal dotted lines show the value of the central perpendicular column density of the Milky Way disk model, adjusted by a factor $1/\cos i$. Bottom row: fitted component velocity offsets relative to $z_{H\alpha}$ for Ca II (left) and Na I (right) absorbers. Systems fit with single velocity components are shown with solid light blue and orange squares. The primary and secondary components of systems fit with two components are shown with filled and open squares outlined in a complementary color. Error bars show the span of velocities included in the Δv_{90} measurement for the Ca II K and Na I 5891 lines. Colored boxes indicate the maximum projected line-of-sight velocity width predicted using simple tilted-ring models with extraplanar layers placed at $z = \pm 0.82$ kpc (for Ca II) and ± 0.43 kpc (for Na II). The maximum rotation velocity (V_∞) of each model is set by the stellar mass Tully-Fisher Relation, and the R_V parameter is varied to model both steeply rising (purple boxes) and gradually increasing (turquoise boxes) rotation curves.

$N(x, y) = \int n(r, z)ds$, with ds representing the differential length element along the line of sight, and with r and z being dependent on s (e.g., Prochaska & Wolfe 1997).

To compute this integral, we adopt a simplified version of the tilted-ring model framework that is commonly used to model H I kinematics and surface brightnesses in disk galaxies (e.g., Rogstad et al. 1974; Bosma 1978; de Blok et al. 2008; Oh et al. 2011; Kamphuis et al. 2015; Oh et al. 2018). In the standard, two-dimensional approach, a galaxy's disk is modeled as a series of concentric ellipses. Each ellipse has an independent central coordinate (x_C, y_C), position angle (ϕ), and inclination (i). Here, we set these parameters to the same value for every ellipse j. To create a three-dimensional model, we replicate this initial set of rings, assigning each set k a thickness $\Delta z = 0.05$ kpc and height z such that the model extends to $z = \pm 10$ kpc. We assign each ring an ionic volume density according to Equation (3) and compute the corresponding column density $N_{j,k} = n_{j,k}\Delta z / \cos i$. We then calculate the (x, y) coordinates of each ring, interpolating the values of $N_{j,k}$ onto a fixed Cartesian grid. Finally, we sum these column densities over all layers to compute $N(x, y)$.

We generate three such models at inclinations $i = 0°$, $50°$, and $75°$. We then compute the range in $N(x, y)$ values predicted at a given $R_\perp = \sqrt{x^2 + y^2}$ for 0 kpc $< R_\perp < 15$ kpc. We show the resulting column density distributions in the upper panels of Figure 13, along with the total system column density measurements for our sample (described in Section 5.2). For reference, we also show the value $N = 2n_0 h / \cos i$ with horizontal dotted lines. For sight lines in which Ca II is securely detected, our measurements are typically well above the maximum column densities predicted for a moderately inclined disk (with $i = 50°$). Even in the extreme case of a disk inclined to $75°$, all six of our sight lines at $R_\perp > 6$ kpc yield Ca II measurements significantly above the projected range of column densities at similarly large impact parameters. Our Na I column densities overall exhibit somewhat greater consistency with our model predictions over the full range of $R_\perp$ of our sample; nevertheless, several of our measurements lie well above those predicted for $i = 50°$.

Given the simplicity of this modeling, as well as our lack of knowledge of the orientation of our foreground galaxy sample,

we cannot use this approach to estimate in detail the contribution of an ISM component to the column densities measured along each sight line. Indeed, the numerous upper limits we place on N(Na I) within $R_\perp < 5$ kpc suggest that our simple model likely overpredicts the Na I column density in some of our foreground systems and/or does not properly capture the patchiness of Na I absorption in the ISM. Moreover, we have assumed here that the volume densities and scale heights of these ions do not vary with overall galaxy stellar mass or SFR. If, for example, volume density is correlated with mass (as obliquely suggested by the findings presented in Section 5.5), our models would tend to overpredict the ISM contribution to the observed column densities, given the stellar mass distribution of our sample. If the volume density of these ions is instead strongly correlated with global SFR, our modeling may underpredict their ISM column densities in light of the analysis presented in Appendix A. However, we emphasize that our model predictions for moderately inclined disks lie well below (>0.9 dex) every measured N(Ca II) value in our sample at $R_\perp > 6$ kpc. We furthermore consider the former scenario to be more likely, given that our empirical constraints on M_* are significantly more secure than those on the global SFRs of our sample.

In view of this likelihood, we interpret the failure of our ISM model to reproduce the large Ca II column densities (as well as the largest Na I column densities) we observe as an indication that there is a significant contribution to these columns from material that is not interstellar. These systems must instead arise at least in part from an extraplanar, or circumgalactic, component. Such absorbers are known to arise in the Milky Way in association with intermediate- and high-velocity H I clouds, which are understood to lie at distances ∼0.5–20 kpc from the disk (Kuntz & Danly 1996; Wakker 2001; Thom et al. 2006; Wakker et al. 2007, 2008). We infer that the phenomena giving rise to these extraplanar or halo clouds are active across our foreground galaxy sample.

6.2. Kinematics

We may also use this framework to predict the distribution of line-of-sight velocities exhibited by the neutral gas disk component of our foreground galaxy sample. We again begin with a single set of tilted rings, assigning each ring a rotation velocity

$$V_{\rm rot}(r) = V_\infty \tanh(r/R_{\rm V}), \qquad (4)$$

with V_∞ equal to the maximum rotation velocity, and $R_{\rm V}$ setting the steepness of the rotation curve in the central regions of the disk. As described in Rogstad et al. (1974) and Begeman (1989), the line-of-sight component of this velocity is $V_{\rm LOS}(x, y) = V_{\rm sys} + V_{\rm rot}(r)\sin i \cos\theta$, with θ representing the azimuthal angle counterclockwise from the major axis in the disk plane, and $V_{\rm sys}$ representing the recession velocity of the system. We then generate two additional, equivalent sets of tilted rings, placing them at heights $z = \pm h$ above and below the first set. This placement ensures that the map of line-of-sight velocity differences ($\Delta V_{\rm LOS}$) between these two layers is representative of the maximum velocity offsets that can be produced by a thick galactic disk exhibiting solid-body rotation.

To generate a kinematic model for each foreground galaxy in our sample, we use the stellar mass Tully-Fisher relation derived by Bloom et al. (2017) from spatially resolved Hα

kinematics of nearby galaxies over the stellar mass range $8.0 < \log M_*/M_\odot < 11.5$ in the SAMI Galaxy Survey (Allen et al. 2015):[18]

$$\log (V_{\rm rot,TF}/{\rm km\,s^{-1}}) = 0.31\log (M_*/M_\odot) - 0.93. \qquad (5)$$

Here, $V_{\rm rot,TF}$ is the velocity measured at $2.2R_{\rm eff}$. This relation was determined from a fit to kinematic data for galaxies with low values of a quantitative asymmetry indicator, and thus may be considered an upper limit on the rotation velocity for lower-M_*, dispersion-dominated systems (Bloom et al. 2017). We calculate the $V_{\rm rot,TF}$ implied by this relation for each foreground galaxy, and then set $V_\infty = V_{\rm rot,TF}$. Because the $R_{\rm V}$ parameter in Equation (4) is unconstrained for our sample, we generate two models for each system, one with $R_{\rm V} = 2$ kpc (creating a steeply rising rotation curve) and one with $R_{\rm V} = 10$ kpc (creating a gradually increasing rotation curve). We compute the distribution of $\Delta V_{\rm LOS}$ for both of these models, assuming $i = 75°$.

Finally, we determine the maximum value of $\Delta V_{\rm LOS}$ predicted at the $R_\perp$ of the corresponding GOTOQ (max[$\Delta V_{\rm LOS}$]). We have indicated these values with colored vertical bars in the bottom panels of Figure 13. Each bar is centered at $\delta v = 0$ km s^{-1} and extends to $\pm$max[$\Delta V_{\rm LOS}$]/2. Note that these bars do not indicate the absolute velocity offset of the material in the layers from $V_{\rm sys}$ (which would extend to many tens of kilometers per second). Instead, because our $z_{\rm H\alpha}$ measurements assess $V_{\rm LOS}(x, y)$ (rather than $V_{\rm sys}$), we are concerned only with the maximum potential velocity offset of extraplanar layers from the former quantity.

As is evident from Figure 13, the magnitude of max[$\Delta V_{\rm LOS}$] increases with increasing M_* and is larger for Ca II relative to Na I due to its larger scale height. This quantity is also to some extent dependent on $R_\perp$, as sight lines that probe locations at which the rotation velocity is increasing steeply with radius are predicted to trace overall larger values of $\Delta V_{\rm LOS}$ (although we find that our predictions are not significantly affected by our choice of $R_{\rm V}$). However, regardless of the mass or $R_\perp$ of the system, we observe both Ca II and Na I absorption over a broader range of velocities than is predicted in this simple framework along nearly every sight line in our sample. The eight sight lines fit with a single Ca II component all exhibit Δv_{90} values (i.e., the span of the error bars in the bottom panels of Figure 13) larger than max[$\Delta V_{\rm LOS}$] by $\geqslant 30$ km s^{-1}. Similarly, the nine sight lines fit with a single Na I component exhibit Δv_{90}(Na I) values greater than the corresponding max[$\Delta V_{\rm LOS}$] by $\geqslant 32$ km s^{-1}. The vast majority of sight lines fit with two Ca II components or two Na I components exhibit component velocity differences ($|\delta v_1 - \delta v_2|$) greater than the predicted max[$\Delta V_{\rm LOS}$] by $\geqslant 20$ km s^{-1}.

The foregoing discussion does not account for the artificial broadening of our observed line profiles due to the finite resolution of our spectrograph (with FWHM ≈ 37.3 km s^{-1}). Prochaska et al. (2008) performed a detailed comparison of Δv_{90} values measured from both ESI and Keck/HIRES spectra of the same QSO sight lines probing foreground damped Lyα systems, finding that Δv_{90} measurements obtained from the ESI spectra were larger than those measured with HIRES by about half the FWHM spectral resolution element. We

---

[18] This relation is derived from stellar masses calculated by Taylor et al. (2011) for the GAMA Survey. This work adopted the same cosmology and the same stellar population synthesis models as used in Straka et al. (2015) for stellar mass estimation.

therefore expect that our Δv_{90} measurements may be biased high by $\approx 19\,\mathrm{km\,s^{-1}}$; however, this level of bias does not reconcile our measurements with the $\max[\Delta V_{\mathrm{LOS}}]$ predictions described above.

In light of the failure of this simple model to reproduce the broad absorption profiles observed, we conclude that the gas kinematics must be broadened by ongoing gas outflow from and/or infall onto the galaxy disks. Moreover, given that the analysis presented in Section 5.3 demonstrated that the bulk of the absorbing material remains within the gravitational potential well of each host, we ascribe the observed motions to Galactic Fountain–like activity. We discuss the novelty and implications of this conclusion in Section 7.3.

7. Discussion

7.1. The Relationship between Absorption Detected along GOTOQ Sight Lines and in Galaxy Spectroscopy

The rest-frame optical wavelengths of the Ca II and Na I transitions studied here have historically made them signatures of choice for studies of the Milky Way ISM (e.g., Hobbs 1969, 1974; Sembach et al. 1993; Welty et al. 1996; Ben Bekhti et al. 2012) and the CGM of nearby galaxies (Boksenberg & Sargent 1978; Boksenberg et al. 1980; Bergeron et al. 1987; Zych et al. 2007; Richter et al. 2011; Zhu & Ménard 2013). Analysis of the Na I D doublet in nearby galaxy spectroscopy has also provided some of the most important evidence for the ubiquity of cold gas outflows among star-forming systems (e.g., Heckman et al. 2000; Schwartz & Martin 2004; Martin 2005; Rupke et al. 2005; Chen et al. 2010b; Roberts-Borsani et al. 2020). Much of the literature focusing on this signature targeted galaxies known to be undergoing starburst activity (e.g., by using an infrared luminosity selection criterion; Heckman et al. 2000; Martin 2005; Rupke et al. 2005), establishing that outflows occur with an incidence that increases with IR luminosity (to $\approx 80\%$ among low-redshift ultraluminous infrared galaxies (ULIRGs); Rupke et al. 2005), and that their typical velocities increase from 10 to $30\,\mathrm{km\,s^{-1}}$ among starbursting dwarfs to 100–$1000\,\mathrm{km\,s^{-1}}$ among ULIRGs (Martin 2005).

Study of Na I outflow signatures in more typical star-forming galaxies was facilitated by the galaxy spectroscopy obtained over the course of the SDSS (e.g., Chen et al. 2010b). While these spectra typically lack the S/N required for analyses of Na I kinematics in individual galaxies, multiple studies have taken the approach of coadding many tens or hundreds of spectra to constrain the mean outflow absorption profile as a function of, e.g., stellar mass, inclination, or specific SFR (e.g., Chen et al. 2010b; Concas et al. 2019).

Figure 14 compares a subset of these findings with some of the results of our GOTOQ study. We focus here on measurements reported by Chen et al. (2010b), as they are most directly comparable to the W_r measured along our GOTOQ sight lines. In detail, Chen et al. (2010b) divided their $z \sim 0.1$ galaxy sample into face-on (with inclinations $i < 60°$) and edge-on ($i > 60°$) subsamples, then binned each of these subsamples by stellar mass over the range $10.3 \lesssim \log M_*/M_\odot < 11.2$. After coadding the spectra in each of these bins, they performed stellar continuum modeling to remove the component of the Na I absorption profile arising in stellar atmospheres. They then modeled the residual Na I absorption with two velocity components: a "systemic" component with a central velocity
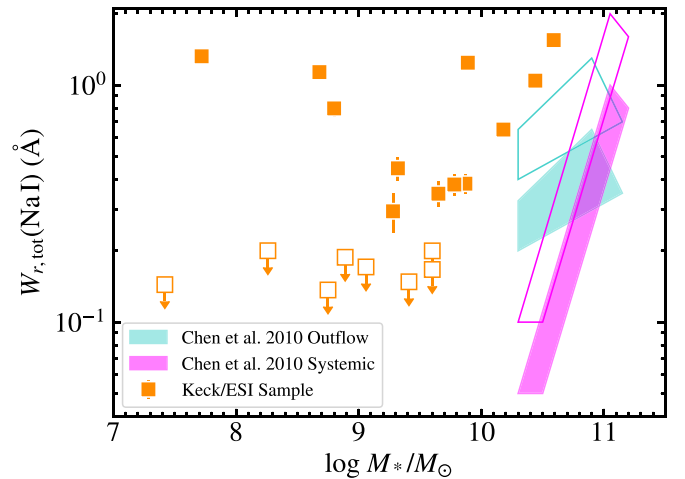
Figure 14. The total system Na I equivalent width ($W_{r,\mathrm{tot}}(\mathrm{Na\,I}) = W_r(\mathrm{Na\,I}\ 5891) + W_r(\mathrm{Na\,I}\ 5897)$) versus $\log M_*/M_\odot$ measured in our ESI spectroscopy. Upper limits, indicated with open squares, are shown in cases in which $W_{r,\mathrm{tot}} < 3\sigma_{W_{r,\mathrm{tot}}}$, and represent 3σ limits. Measurements of GOTOQJ0851 +0791 have been excluded, as the Na I 5897 profile in that sight line is contaminated by blending. The turquoise and magenta filled regions show the distribution of W_r values measured by Chen et al. (2010b) in coadded SDSS galaxy spectra for the blueshifted and systemic components of the Na I absorption profile, respectively. The open regions show the locus of values covered by the Chen et al. (2010b) measurements if they are corrected upward by a factor of two to account for the potential contribution of material located on the far side of the stellar continua.

fixed to that of the system and an "outflow" component with a central velocity that was allowed to vary freely. They reported the total W_r (including both doublet lines) of the systemic components ($W_{r,\mathrm{systemic}}$) fit to their edge-on subsamples, and reported the total W_r of the outflow components ($W_{r,\mathrm{outflow}}$) fit to their face-on subsamples. The approximate parameter space covered by these measurements as a function of M_* is indicated in Figure 14 with filled magenta and turquoise shapes, respectively. Chen et al. (2010b) note that both $W_{r,\mathrm{systemic}}$ and $W_{r,\mathrm{outflow}}$ increase strongly with M_*, and these trends are reflected in the overall slopes of these regions. Here we compare these values with the total Na I rest equivalent width $W_{r,\mathrm{tot}}(\mathrm{Na\,I}) = W_r(\mathrm{Na\,I}\ 5891) + W_r(\mathrm{Na\,I}\ 5897)$ measured along each of our sight lines (excluding GOTOQJ0851+0791, for which one of the doublet lines is severely blended).

This comparison reveals that all foreground galaxies in our sample having stellar masses within or close to the range studied by Chen et al. (2010b) exhibit higher values of $W_{r,\mathrm{tot}}(\mathrm{Na\,I})$ than were measured in either the outflowing or systemic components of systems with comparable M_* values. In detail, we consider here the five GOTOQs having $\log M_*/M_\odot > 9.8$. Our measurements for four of these systems are close to a factor of 10 higher than $W_{r,\mathrm{systemic}}$ at approximately equivalent stellar masses, and are ≈ 0.4–$1.0\,\mathrm{\mathring{A}}$ higher than $W_{r,\mathrm{outflow}}$. This offset may be due in part to the different experimental designs of these two studies: our QSO sight lines probe all absorption along the line of sight, both behind and in front of the foreground host; whereas down-the-barrel spectroscopy is sensitive only to material foreground to the galaxy's stellar populations. We posit that were we able to use down-the-barrel spectroscopy to probe material arising on the *far* side of the galaxies' stellar components (i.e., the gas along the line of sight that is beyond the galaxies' stars from the point of view of the observer), this would result in a potential increase in the observed W_r by a factor of two (as indicated with the open regions in Figure 14). This is likely an overestimate, particularly for

$W_{r,\mathrm{systemic}}$, as saturated absorbing components with velocities that overlap those observed on the front side would not add to the observed total equivalent width. Even so, our GOTOQ $W_{r,\mathrm{tot}}$ values still lie well above the predicted equivalent widths implied by the Chen et al. (2010b) measurements.

The $3''$ diameter fibers used for the SDSS spectroscopy extend to radii of $R_\perp = 2.5\,\mathrm{kpc}$ at the median redshift of the Chen et al. (2010b) sample ($z = 0.09$), whereas the five GOTOQs relevant to this comparison are being probed at impact parameters $R_\perp = 3.4, 3.4, 4.0, 7.5$, and $10.6\,\mathrm{kpc}$, or $R_\perp/R_{\mathrm{eff,est}} = 0.5, 1.5, 0.7, 0.7$, and 1.6. While these sight lines are not passing through the galaxy centers, they are nevertheless likely probing star-forming regions in their disks. The elevated absorption strengths we observe may imply either that (1) there is a significant contribution to the GOTOQ Na I profiles from inner halo material distributed toward the galaxy outskirts, (2) our GOTOQ sight lines do not fully sample the distribution of $W_{r,\mathrm{tot}}(\mathrm{Na\,I})$ values for the galaxy population as a whole due to their small numbers, or (3) the Chen et al. (2010b) absorption strengths are suppressed due to resonantly scattered Na I emission or to overestimation of the contribution of stellar atmospheres to the coadded line profiles.

Galactic fountain models invoking feedback-driven condensation and cooling of material from hot coronal gas may provide a theoretical explanation for the putative detection of excess cold clouds located close to the disk but at projected separations of $> 0.5\,R_\perp/R_{\mathrm{eff}}$ from a galaxy's axis of symmetry (Marasco et al. 2012; Fraternali et al. 2013). However, given our relatively small sample, this data set cannot distinguish between the three scenarios laid out above. We simply note here that Na I emission from scattering has been found to be weakest in edge-on galaxies and thus should have a minimal effect on $W_{r,\mathrm{systemic}}$ (Chen et al. 2010b; Roberts-Borsani et al. 2020). In addition, some degree of "contamination" of the spectral libraries used to model the stellar continuum by interstellar material in the Milky Way remains a distinct possibility. Comparison to continuum models constructed from purely theoretical stellar spectra suggests this can result in an underestimate of the $W_{r,\mathrm{tot}}(\mathrm{Na\,I})$ arising from the ISM of ≈ 0.5–$0.7\,\text{Å}$ (K. S. Parker et al 2022, in preparation).

Finally, we comment that the opposite effect has been found in comparisons of the W_r of outflows traced by Mg II $\lambda\lambda 2796$, 2803 absorption in galaxy spectra (Rubin et al. 2014) to the strength of circumgalactic Mg II absorption at impact parameters $10\,\mathrm{kpc} \lesssim R_\perp \lesssim 170\,\mathrm{kpc}$ (Chen et al. 2010a). The enhanced $W_r(\mathrm{Mg\,II})$ detected down-the-barrel relative to those typically detected along QSO sight lines suggests that the bulk of the outflowing material does not reach distances of more than $\sim 10\,\mathrm{kpc}$. The $W_r(\mathrm{Mg\,II})$ values measured along GOTOQ sight lines at impact parameters $R_\perp < 6\,\mathrm{kpc}$ by Kacprzak et al. (2013) are closer in strength to those observed in galaxy spectra ($1.75\,\text{Å} < W_r(\mathrm{Mg\,II}\ 2796) < 3.11\,\text{Å}$), implying that the region ~ 6–$10\,\mathrm{kpc}$ from a galaxy's center may be an important interface for the stalling of Mg II-absorbing wind material. Comparison of our $W_r(\mathrm{Na\,I})$ measurements to the Chen et al. (2010b) results places no such constraint on the potential extent of Na I-absorbing winds.

7.2. The Relationship between $\mathrm{W_r}$(Ca II K) and Star Formation

We identified a strong, statistically significant correlation between $W_r(\mathrm{Ca\,II\,K})$ and the local SFR of the absorber host measured within the SDSS fiber (see Figure 11). To our knowledge, our study presents the first evidence for such a relationship (although a correlation between Hα flux and $W_r(\mathrm{Ca\,II\,K})$ was noted in Straka et al. 2015). However, evidence that strong Ca II absorbers have significant dust content was uncovered more than a decade ago (Wild & Hewett 2005; Zych et al. 2009). By coadding SDSS QSO spectra in the rest frame of strong Ca II systems, Wild et al. (2007) detected and characterized associated [O II] $\lambda\lambda 3727$, 3729 emission arising within the SDSS fibers, measuring an average SFR of 0.1–$0.5\,M_\odot\,\mathrm{yr}^{-1}$. Additional evidence for a connection with star formation was contributed by Zhu & Ménard (2013), whose stacking analysis detected a stronger mean Ca II absorption signal in the halos of star-forming galaxies relative to red-sequence hosts at fixed stellar mass.

The relation is reminiscent of the now well-established evidence for a correlation between Mg II absorption strength and SFR. This is seen both in down-the-barrel studies (Bordoloi et al. 2014; Rubin et al. 2014), as well as in QSO absorption-line systems and in QSO–galaxy pair experiments. Ménard et al. (2011) assessed the [O II] luminosity of Mg II absorbers as a function of their W_r, reporting a 15σ correlation between these quantities, and showing that the distribution function of $W_r(\mathrm{Mg\,II})$ can be related to the [O II] luminosity function using a simple scaling. Lan et al. (2014) studied the host galaxy properties of Mg II absorbers detected in the SDSS QSO sample as a function of their W_r, finding that stronger absorbers are surrounded by higher numbers of star-forming galaxies within $R_\perp < 50\,\mathrm{kpc}$. Lan & Mo (2018) confirmed this connection, measuring larger average $W_r(\mathrm{Mg\,II})$ within $50\,\mathrm{kpc}$ of emission-line galaxies selected from SDSS-IV/eBOSS with higher SFRs.

Taken together, these studies provide strong evidence for star formation activity as a primary origin of strong Mg II absorption. Our findings, together with the literature reviewed above, are suggestive of a similarly strong link between star formation and Ca II-absorbing material, which in turn implies that Ca II may prove an effective tracer of winds in down-the-barrel studies. Very few such works have made use of Ca II H & K for this purpose, due to the blue spectral coverage required, as well as to the strength of these transitions in stellar atmospheres and the potential for confusion from Hϵ $\lambda 3971$ line emission. However, if these systematics could be successfully mitigated via detailed stellar population and emission-line modeling (e.g., Westfall et al. 2019), Ca II may prove a useful probe of the spatially resolved outflow kinematics of warm, neutral gas in advance of the availability of UV-sensitive IFUs that will map the motions of more highly ionized material in absorption (e.g., Tumlinson et al. 2019).

7.3. Galactic Fountains in External Galaxies

The Galactic Fountain model was originally introduced to explain the origin of high-velocity clouds (HVCs) of H I in the Milky Way halo (Shapiro & Field 1976). In this picture, a dynamic, hot corona is continually fed and heated by supernova ejecta. Material lofted above the disk rises and cools, moving outward radially along the pressure gradient of the corona. Thermal instabilities trigger the condensation of neutral clouds from the hot gas, which purportedly fall back toward the disk on ballistic trajectories. There have been numerous theoretical investigations exploring the implications of this model for the ionized component of Milky Way HVCs (e.g., Marasco et al. 2013), the metallicities of HVCs (Marasco & Fraternali 2017),

and the X-ray emitting properties of the Milky Way's coronal plasma (Joung & Mac Low 2006; Henley et al. 2015).

A now significant body of theoretical work has also invoked this model to predict the properties of the gaseous components of external galaxies. Surveys of 21 cm H I emission in nearby star-forming systems having rotation velocities $\gtrsim 80$ km s^{-1} have revealed ubiquitous extraplanar layers of neutral gas that extend to $\gtrsim 1$ kpc above the disk plane (van der Hulst & Sancisi 1988; Fraternali et al. 2002; Oosterloo et al. 2007; Marasco et al. 2019), and that typically lag behind the disk rotation speed (Fraternali et al. 2002; Barbieri et al. 2005). This "anomalous" component arises within the inner few kiloparsecs of the disk, and has typical masses of $\sim 10^{8\text{-}9}$ $M_\odot$ (Marasco et al. 2019). Fraternali & Binney (2008) argued against an external (or circumgalactic) origin for this material, given that if it were to fall onto the host galaxy disks over a freefall time, the implied accretion rates would be orders of magnitude larger than the SFRs of nearby spirals. This inconsistency in itself is strongly suggestive of a fountain origin for extraplanar H I gas (Fraternali & Binney 2008; Marasco et al. 2019). While models that adopt purely ballistic trajectories for supernova ejecta fail to reproduce the observed lag in the rotation of extraplanar layers (Fraternali & Binney 2006), a modification of these models that accounts for the interaction between feedback-driven outflow and cool accretion flows successfully explains both the surface brightness and kinematics of the extraplanar material in the two well-studied spirals NGC 891 and NGC 2403 (Fraternali & Binney 2008).

The models described above adopt a Gaussian distribution for the velocities of clouds ejected from the galactic disk, with the dispersion adjusted to achieve the closest match between the predicted and observed H I surface brightnesses. Another common approach to the modeling of extraplanar H I layers is to adopt a single value for the layer velocity perpendicular to the disk (e.g., Marasco et al. 2019). Both approaches predict velocity widths of $\gtrsim 50$–150 km s^{-1} along individual lines of sight through 21 cm emission-line maps of moderately inclined galaxies (Marasco et al. 2019). The Δv_{90} widths we have measured imply similar velocity spreads of >50–180 km s^{-1} across our sample, over the full range of impact parameters we probe ($R_\perp = 1 - 13$ kpc).

We have seen from the analysis presented in Section 6.2 that these velocity widths far exceed those predicted for the interstellar component of these galaxies. Instead, they are qualitatively consistent with the kinematics predicted by commonly invoked fountain models. Our line profile modeling additionally demonstrates that these velocity widths frequently arise from multiple, distinct structures (i.e., components) with velocity offsets of >40 km s^{-1}, and arise from both the warm neutral material traced by Ca II and a colder phase traced by Na I. Furthermore, whereas extraplanar H I is typically well fit by models that adopt exponential scale lengths of $R_g = 1$–7 kpc for the surface density of the layer (i.e., $\Sigma(R) \propto e^{R/R_g}$; Marasco et al. 2019), our absorption velocity widths suggest that the physical processes driving galactic fountain flows persist to $R_\perp \sim 7$ kpc and beyond.

Finally, we emphasize the novel stellar mass distribution of our sample in this context: six of the 14 foreground galaxies giving rise to securely detected Ca II have M_* values that imply rotation velocities in the range $V_{\rm rot,TF} = 20$–80 km s^{-1}. The consistently high Δv_{90} values we measure across this parameter

space provide novel evidence for galactic fountain activity in such low-mass systems.

A handful of alternative observational approaches have offered additional evidence for galactic fountain flows in external galaxies. The Hα and radio continuum emission from the extraplanar layers of the nearby edge-on spiral NGC 891, along with the properties of the dust complexes that pervade them, have long been interpreted as consistent with galactic fountain model predictions (Dettmar 1990; Rand et al. 1990; Bregman & Houck 1997; Howk & Savage 1997; Kamphuis et al. 2007). These studies also offer direct evidence for the multiphase nature of the galactic fountain material, with dust-bearing clouds likely tracing a similar phase to that giving rise to Na I (Howk & Savage 2000). Such multiphase "interstellar thick disks" are now known to be ubiquitous (Zschaechner & Rand 2015; Boettcher et al. 2016; Bizyaev et al. 2017; Li et al. 2021) and are observed to exhibit metallicities ranging from a factor of two lower than the host galaxy disk to slightly above that observed in the host (e.g., Howk et al. 2018). Most recently, Rupke et al. (2021) took advantage of echellette-resolution optical IFU spectroscopy of eight nearby AGN-dominated galaxies to trace the down-the-barrel kinematics of these layers, identifying ongoing outflow and inflow in nearly every system via the Doppler shift of Na I, with the projected areas subtended by these flows covering up to 25% of the optically bright stellar disks.

Modern theoretical studies of galactic fountain flows have used high-resolution numerical simulations to make detailed predictions for the temperature distribution and kinematics of extraplanar material, drawing physical links between recent-past star formation activity and the launch of expanding superbubbles (e.g., Creasey et al. 2013; Girichidis et al. 2016; Martizzi et al. 2016; Kim & Ostriker 2018; Kado-Fong et al. 2020; Vijayan et al. 2020). While the vast majority of these studies do not simulate material in the coolest phases traced by Na I, recent work by Girichidis et al. (2021) and Farber & Gronke (2021) investigated the formation and survival of such cool, dust-enshrouded material explicitly. The former study found that magnetized, hot wind material can effectively trigger the condensation of a molecular phase from a high-density ($n \gtrsim 0.5$ cm^{-3}), warm ($T \sim 10^{3\text{-}4}$ K) cloud (Girichidis et al. 2021), while the latter found that this phase can survive over numerous cloud-crushing times if the cloud is sufficiently large, and that dust grains can likewise survive in $\gtrsim 100$ pc clouds if the temperature for dust destruction $T_{\rm dest} > 10^4$ K (Farber & Gronke 2021). These theoretical advances, along with ongoing efforts to link the results of parsec-resolution numerical simulations of galactic disks to simulations encompassing dark matter halo scales (e.g., SMAUG; Kim et al. 2020), will enable detailed comparison of the predictions of these models to the observed kinematics and absorption/emission-line strengths of extraplanar material. Such comparisons are crucial to affirming these theoretical efforts, as the associated predictions have not yet been rigorously compared to the numerous in-hand observational constraints.

8. Summary and Conclusions

We have analyzed medium-resolution optical spectroscopy of 21 bright quasars known a priori to lie exceptionally close to foreground galaxies having redshifts $0.03 < z < 0.20$ with the purpose of assessing the strength and kinematics of Ca II H & K and Na I $\lambda\lambda 5891, 5897$ absorption arising in their ISM and

disk–halo interface. The foreground systems were identified serendipitously via intervening nebular emission lines in SDSS spectra of the quasars by Straka et al. (2013, 2015), who located their photometric counterparts in SDSS imaging and measured impact parameters in the range 1 kpc $< R_\perp <$ 13 kpc. The foreground galaxies span a broad range of stellar masses ($7.4 \leqslant \log M_*/M_\odot \leqslant 10.6$), and the strength of the Hα emission detected in the SDSS fibers implies that their global SFRs lie both within and well above the star-forming sequence at $z \sim 0$. Our spectroscopy, with a velocity resolution FWHM ≈ 37.3 km s^{-1}, is sensitive to absorbers having W_r(Ca II K) $\gtrsim 0.2$ Å and W_r(Na I 5891) $\gtrsim 0.15$ Å. We used Voigt profile modeling to derive column densities, Doppler parameters, and component velocities for each securely detected system. We also calculated a nonparametric measure of the profile velocity widths (Δv_{90}). Our analysis has revealed the following:

1. We find no evidence for an anticorrelation between the W_r values we measure and either $R_\perp$ or $R_\perp/R_{\rm eff,est}$ (i.e., the impact parameter normalized by an estimate of the effective radius of the foreground host galaxy). Modeling of the relation between $\log W_r$(Ca II K) (or $\log W_r$(Na I 5891)) and either measure of projected separation as linear yields slopes that do not significantly differ from zero. This is unusual in the context of the QSO–galaxy pair studies literature, which, in the vast majority of cases, report statistically significant anticorrelations between W_r and $R_\perp$ at larger impact parameters than we probe (15 kpc $\lesssim R_\perp \lesssim 100$ kpc).

2. Strong absorption with column densities N(Ca II) $> 10^{12.5}$ cm^{-2} (N(Na I) $> 10^{12.0}$ cm^{-2}) occurs with an incidence f_C(Ca II) $= 0.63^{+0.10}_{-0.11}$ (f_C(Na I) $= 0.57^{+0.10}_{-0.11}$) within our sample. We find no evidence for a dependence of these covering fractions on $R_\perp$ or $R_\perp/R_{\rm eff,est}$. These f_C values are consistent with the incidence of significantly weaker intermediate- and high-velocity Ca II and Na I absorbers (with N(Ca II) $> 10^{11.4}$ cm^{-2} and N(Na I) $> 10^{10.9}$ cm^{-2}) detected in the Milky Way (Ben Bekhti et al. 2012). This implies that our sight lines exhibit overall stronger absorption than those probing Milky Way extraplanar/halo clouds, likely due to their longer path lengths through both the ISM and CGM.

3. The velocities of our Ca II and Na I component samples exhibit overall small offsets relative to the Hα emission velocities measured along the same sight lines ($z_{\rm H\alpha}$). Among 20 Ca II (and 17 Na I) components, only three (one) have fitted relative velocities $|\delta v| > 50$ km s^{-1}. The portions of each line profile contributing 90% of the apparent optical depth all extend to a maximum $\delta v < 120$ km s^{-1} and, thus, trace material that must remain gravitationally bound to even the lowest-M_* system in the sample. However, the corresponding Δv_{90} widths lie in the range 50–180 km s^{-1}, indicating the absorption has contributions from both interstellar and extraplanar material.

4. We find no evidence for a correlation between the dust reddening measured along our QSO sight lines and the W_r of the Ca II K or Na I 5891 transitions. Between a quarter and a third of our absorber sample are 3σ outliers from the best-fit relations between these quantities

measured toward extragalactic probes of the Milky Way halo.

5. We find no evidence for a strong dependence of the W_r of either ion on the M_* of our foreground galaxies. Instead, we measure an overall high incidence of $W_r > 0.2$ Å absorbers ($f_C \sim 0.4$–0.6) across the full M_* range of our sample. We additionally report a significant ($>3\sigma$) correlation between W_r(Ca II K) and the local SFR implied by the Hα emission-line luminosity measured from SDSS fiber spectra of the sight lines. These findings suggest that (1) Na I is an effective probe of disk–halo gas kinematics across the full M_* range of our sample, and that (2) down-the-barrel spectroscopy of the Ca II transition will be sensitive to star formation-driven outflows of warm, neutral gas.

The Na I absorption strengths we measured along our sample sight lines are significantly larger than the W_r of either outflowing or interstellar material close to the systemic velocity measured in coadded SDSS spectra of galaxies with similar stellar masses. In addition, our measured column densities of both Ca II and Na I are too large to arise from a Milky Way–like ISM. Instead, the columns and large velocity widths ($\Delta v_{90} = 50 - 180$ km s^{-1}) of these absorbers require a significant contribution from material with velocities offset by $\delta v > 20$ km s^{-1} from the galaxies' H II regions, but which is gravitationally bound to each system.

Galactic Fountain models provide a natural explanation for these kinematics and column densities at least in a qualitative sense. Assuming this interpretation is apt, our analysis provides novel evidence for Galactic Fountain activity in low-M_*, nearby galaxies. It further suggests that fountain-driven gas motions arise at large projected separations from the nuclei of the host galaxies ($R_\perp \gtrsim 7$ kpc). While some groups are now pursuing important, direct comparison between fountain flows as observed in 21 cm emission and H I emission-line kinematics predicted in cosmological simulations (e.g., El-Badry et al. 2018; Oman et al. 2019; Watts et al. 2020; Manuwal et al. 2021), the QSO absorption-line measurements we present here offer a complementary, and in some ways simpler, point of comparison for Galactic Fountain model predictions. Such comparisons are crucial to improving our understanding of the cycling of multiphase gas flows through galaxy disks.

Appendix A
On the Effects of Fiber Losses

Our sample of foreground galaxies was identified from the serendipitous overlap of associated H II regions with a nearby SDSS fiber pointing. This implies that the nebular emission flux captured by the fiber may be a small fraction of the total line flux emitted by the host galaxy. Moreover, the fibers with the largest angular separations from the centers of the associated hosts are likely to include smaller fractions of the total line flux than their counterparts at the closest angular separations. Here we build simple models of the H II region emission arising from each galaxy to assess the potential impacts of these limitations on our analysis.

We begin by assuming that the nebular emission from each galaxy is uniformly distributed in an exponentially declining disk with a half-light radius equal to the $R_{\rm eff,est}$ we derived in Section 3, and with a disk thickness $dz = 50$ pc. This model does not account for morphological disturbances, nor for the

small-scale variation in H II region properties observed at very high spatial resolutions (e.g., Kreckel et al. 2018). However, given the relatively low spatial resolution of the fiber observations (with typical seeing FWHM $\sim 1\rlap{.}''32$[19]), we posit that these assumptions will provide a useful assessment of systematics in spite of their simplicity. We draw on the tilted-ring modeling framework discussed in Section 6 to construct each disk with a single layer of rings, adopting a scale radius $R_{\rm S} = R_{\rm eff,est}/1.678$ (Ciotti & Bertin 1999). We further assume that the surface brightness of the nebular emission (e.g., from Hα) is directly proportional to the local star formation rate surface density ($\Sigma_{\rm SFR}$), so that we may write the radial profile of this quantity as $\Sigma_{\rm SFR}(r) = \Sigma_{\rm SFR,0} e^{-r/R_{\rm S}}$. The total SFR of this system can then be written $\mathrm{SFR_{tot}} = \Sigma_{\rm SFR,0} R_{\rm eff,est} \frac{2\pi}{1.678^2}\Gamma(2)$, as described in Ciotti & Bertin (1999).

For each foreground galaxy, we set $\Sigma_{\rm SFR,0}$ to an arbitrary value (0.1 $M_\odot$ yr^{-1} kpc^{-2}), and generate the resulting $\Sigma_{\rm SFR}$ distribution as observed both face-on (with $i = 0°$) and at an inclination of $i = 75°$ (using the same approach described in Section 6.1). We then smooth these distributions with a two-dimensional Gaussian kernel having FWHM $= 1\rlap{.}''32$ to simulate the effects of seeing. Finally, we "observe" these distributions with a 3″ diameter fiber placed at a distance $R_\perp$ from the center of the model, adopting position angles spanning between PA $= 0°$ and 170° at intervals of 10°. We sum the model star formation activity falling within each fiber pointing, and normalize this quantity by the corresponding $\mathrm{SFR_{tot}}$.

This fraction is shown in the left panel of Figure 15 versus $R_\perp$. The rose-colored horizontal dash indicates the fraction of $\mathrm{SFR_{tot}}$ observed in these fibers in the face-on ($i = 0°$) case, and the vertical turquoise lines mark the range of values observed around systems oriented with $i = 75°$. The right-hand panel of this figure shows the value of $\mathrm{SFR_{local}}$ for each system (with magenta squares), as well as the range of $\mathrm{SFR_{tot}}$ values implied by the fractions shown at left. For systems having $R_\perp < 5$ kpc, our modeling suggests that the SDSS fibers include $\gtrsim 10\%$ of the total line emission associated with star formation in a majority of cases (eight out of 11). For systems having $R_\perp > 5$ kpc, the SDSS fibers may exclude $\gtrsim 90\%$–99% of the total nebular line emission. This implies that the $\mathrm{SFR_{tot}}$ values of a handful of our foreground systems (≈ 7 of the 17 shown here) may be quite large ($\gtrsim 10$–100 $M_\odot$ yr^{-1}). Such high global SFRs would place them well above the star-forming sequence at $z \sim 0$ shown in Figure 2. Moreover, under the assumption that highly star-forming galaxies have stronger interstellar and circumgalactic Na I and Ca II absorption overall, the higher frequency of such systems observed at larger impact parameters may drive the log W_r–$R_\perp$ relations we fit in Section 5.1 to have shallower slopes.

---

[19] Assessment of the spatial resolution of the final SDSS imaging data is provided at https://www.sdss.org/dr14/imaging/other_info/.
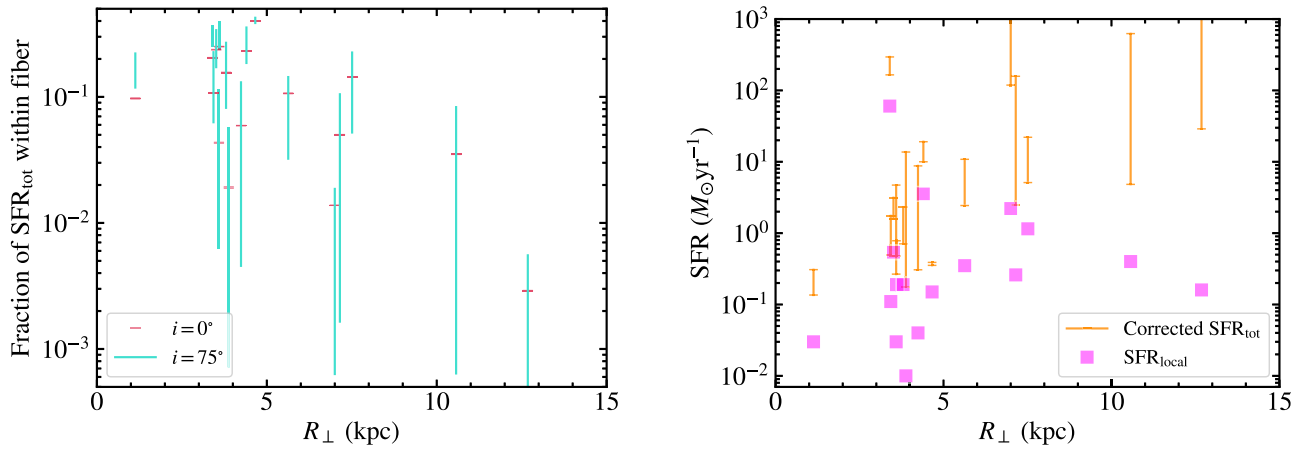
Figure 15. Left: the fraction of the total SFR of each foreground galaxy probed by the corresponding SDSS fiber, as implied by our exponential disk modeling. The rose-colored horizontal dashes indicate the fraction of H II region emission observed if the galaxy is viewed face-on, while the vertical turquoise lines show the range in this observed fraction in the case that the galaxy is oriented close to edge-on with $i = 75°$ (accounting for uncertainty in the positional angle of the fiber placement). Right: the SFR_{local} measured in each fiber observation (magenta squares) vs. $R_\perp$. The ranges indicated in orange show the span of SFR_{tot} values implied by the fractions shown at left.

Because of the significant degree of uncertainty in these estimates (due to, e.g., uncertainties in viewing angle, uncertainties in the position angle of the fiber observations relative to the major axis of each galaxy, and the simplicity of our assumptions regarding the spatial distribution of star formation activity), we do not explicitly fold them into our analyses of the relationships between absorber properties and star formation rate. As emphasized in Section 5.5, we have focused solely on the relation between SFR_{local}, which is well measured by the SDSS fiber spectroscopy at our disposal, and

absorber strength and kinematics. The analysis presented here serves to better contextualize our sample within the broader galaxy population.

Appendix B
Sample Spectroscopy

Figure 16 shows our spectroscopy of GOTOQ sight lines that are not included in Figure 3.
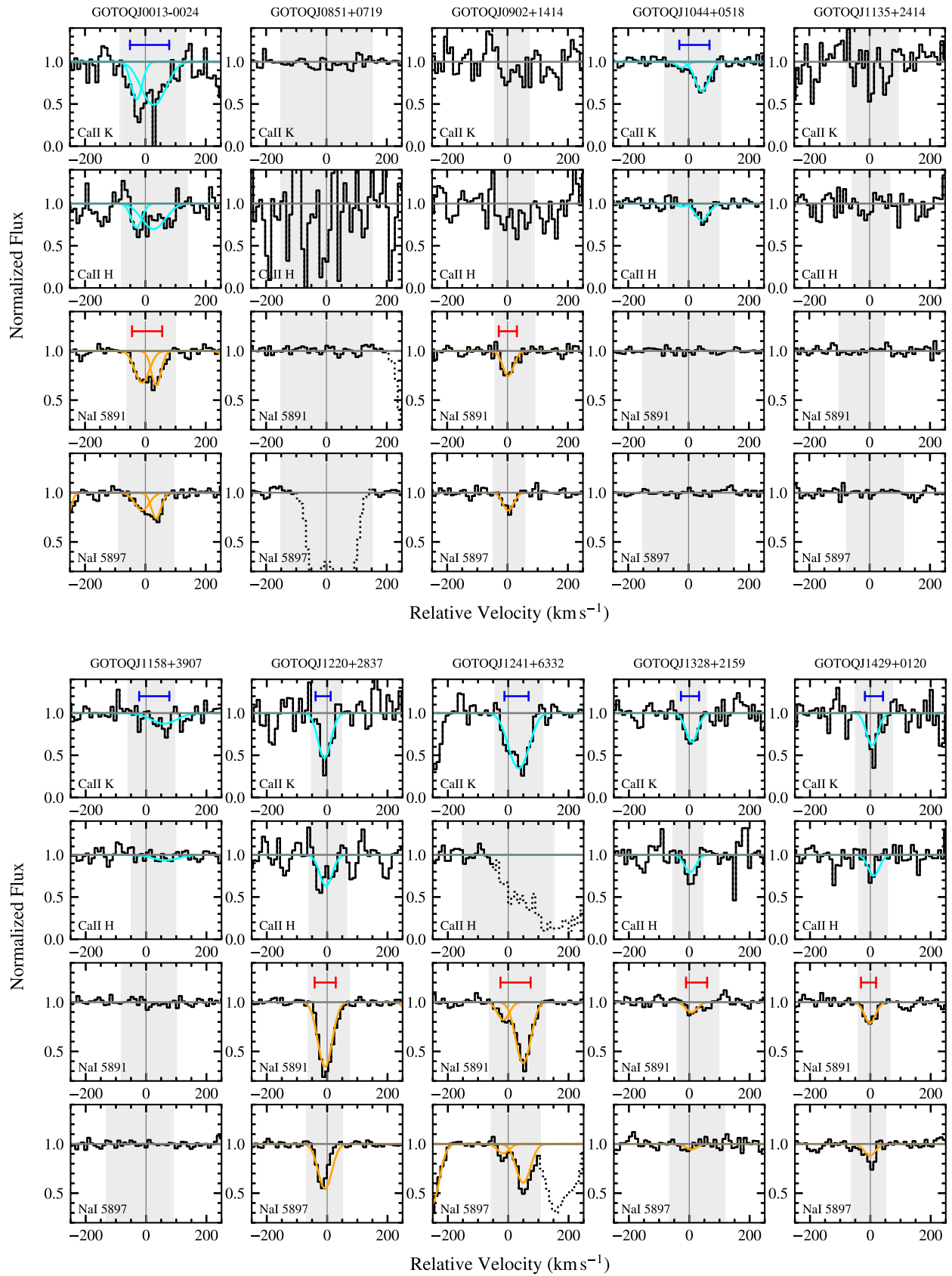
Figure 16. ESI GOTOQ spectra showing the locations of the Ca II H & K and Na I $\lambda\lambda5891$, 5897 transitions in the rest frame of the foreground galaxy. The velocity is defined relative to the GOTOQ redshift estimated from a Gaussian fit to its Hα emission as described in Section 4.1 ($z_{H\alpha}$). The gray horizontal line indicates the continuum level, and the gray shaded region shows the velocity window selected for computation of W_r, N_{aod}, and Δv_{90}. Absorption from unassociated blends is shown with a dotted histogram. The blue and red bars show the pixels that contain >5% of the total apparent optical depth of the line (determined by stepping inward from the profile edges), and the length of these bars corresponds to Δv_{90}. Best-fit profile models are shown with cyan (for Ca II) and orange (for Na I) curves for systems with significantly detected absorption (see Section 4.2 for details).
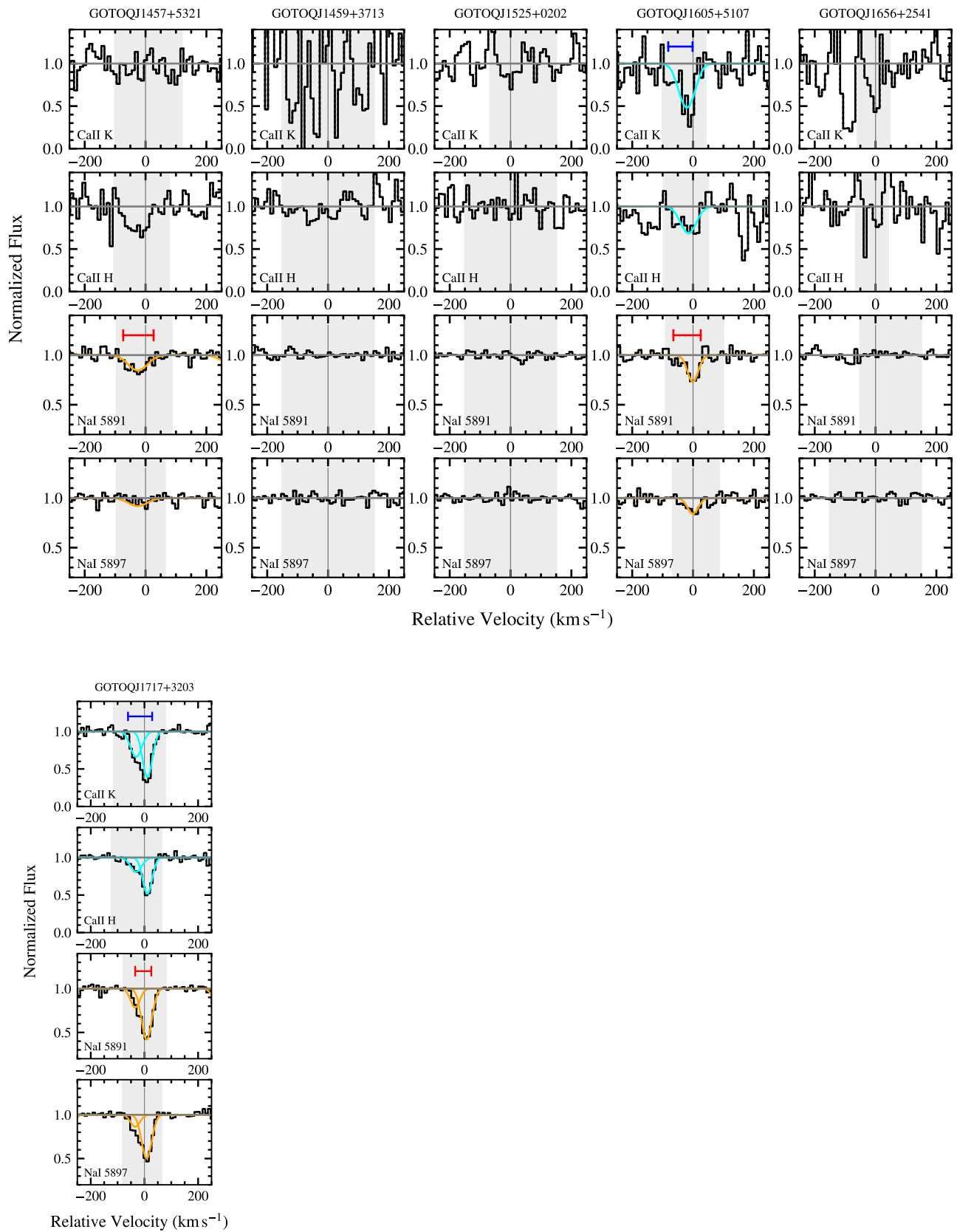
Figure 16. (Continued.)

ORCID iDs

Kate H. R. Rubin ⦿ https://orcid.org/0000-0001-6248-1864
Kathy L. Cooksey ⦿ https://orcid.org/0000-0001-5810-5225
Jessica K. Werk ⦿ https://orcid.org/0000-0002-0355-0134
J. Xavier Prochaska ⦿ https://orcid.org/0000-0002-7738-6875
John M. O'Meara ⦿ https://orcid.org/0000-0002-7893-1054
Joseph N. Burchett ⦿ https://orcid.org/0000-0002-1979-2197
Ryan J. Rickards Vaught ⦿ https://orcid.org/0000-0001-9719-4080
Varsha P. Kulkarni ⦿ https://orcid.org/0000-0002-2587-2847
Lorrie A. Straka ⦿ https://orcid.org/0000-0001-5892-6760

References

Abazajian, K. N., Adelman-McCarthy, J. K., Agüeros, M. A., et al. 2009, ApJS, 182, 543
Ahumada, R., Prieto, C. A., Almeida, A., et al. 2020, ApJS, 249, 3
Allen, J. T., Croom, S. M., Konstantopoulos, I. S., et al. 2015, MNRAS, 446, 1567
Astropy Collaboration, Price-Whelan, A. M., & Sipőcz, B. M. 2018, AJ, 156, 123
Astropy Collaboration, Robitaille, T. P., Tollerud, E. J., et al. 2013, A&A, 558, A33
Bajaja, E., Cappa de Nicolau, C. E., Cersosimo, J. C., et al. 1985, ApJS, 58, 143
Barbieri, C. V., Fraternali, F., Oosterloo, T., et al. 2005, A&A, 439, 947
Baron, D., Stern, J., Poznanski, D., & Netzer, H. 2016, ApJ, 832, 8
Begeman, K. G. 1989, A&A, 223, 47
Begum, A., Chengalur, J. N., Karachentsev, I. D., Sharina, M. E., & Kaisin, S. S. 2008, MNRAS, 386, 1667
Ben Bekhti, N., Richter, P., Westmeier, T., & Murphy, M. T. 2008, A&A, 487, 583
Ben Bekhti, N., Winkel, B., Richter, P., et al. 2012, A&A, 542, A110
Bergeron, J., D'Odorico, S., & Kunth, D. 1987, A&A, 180, 1
Bergeron, J., & Stasińska, G. 1986, A&A, 169, 1
Bish, H. V., Werk, J. K., Peek, J., Zheng, Y., & Putman, M. 2021, ApJ, 912, 8
Bish, H. V., Werk, J. K., Prochaska, J. X., et al. 2019, ApJ, 882, 76
Bizyaev, D., Walterbos, R. A. M., Yoachim, P., et al. 2017, ApJ, 839, 87
Blades, J. C., Hunstead, R. W., & Murdoch, H. S. 1981, MNRAS, 194, 669
Bland-Hawthorn, J., Veilleux, S., Cecil, G. N., et al. 1998, MNRAS, 299, 611
Bloom, J. V., Croom, S. M., Bryant, J. J., et al. 2017, MNRAS, 472, 1809
Boettcher, E., Zweibel, E. G., Gallagher, J. S. I., & Benjamin, R. A. 2016, ApJ, 832, 118
Bohlin, R. C., Savage, B. D., & Drake, J. F. 1978, ApJ, 224, 132
Boksenberg, A., Danziger, I. J., Fosbury, R. A. E., & Goss, W. M. 1980, ApJL, 242, L145
Boksenberg, A., & Sargent, W. L. W. 1978, ApJ, 220, 42
Bolzonella, M., Miralles, J. M., & Pelló, R. 2000, A&A, 363, 476
Bordoloi, R., Lilly, S. J., Hardmeier, E., et al. 2014, ApJ, 794, 130
Bosma, A. 1978, PhD thesis, Groningen University
Bregman, J. N. 1980, ApJ, 236, 577
Bregman, J. N., & Houck, J. C. 1997, ApJ, 485, 159
Brinchmann, J., Charlot, S., White, S. D. M., et al. 2004, MNRAS, 351, 1151
Broeils, A. H., & Rhee, M. H. 1997, A&A, 324, 877
Bruch, R. J., Gal-Yam, A., Schulze, S., et al. 2021, ApJ, 912, 46
Burchett, J. N., Tripp, T. M., Bordoloi, R., et al. 2016, ApJ, 832, 124
Chen, H.-W., Helsby, J. E., Gauthier, J.-R., et al. 2010a, ApJ, 714, 1521
Chen, Y.-M., Tremonti, C. A., Heckman, T. M., et al. 2010b, AJ, 140, 445
Cherinka, B., & Schulte-Ladbeck, R. E. 2011, AJ, 142, 122
Ciotti, L., & Bertin, G. 1999, A&A, 352, 447
Concas, A., Popesso, P., Brusa, M., Mainieri, V., & Thomas, D. 2019, A&A, 622, A188
Cooper, J. L., Bicknell, G. V., Sutherland, R. S., & Bland-Hawthorn, J. 2008, ApJ, 674, 157
Crawford, I. A. 1992, MNRAS, 259, 47
Creasey, P., Theuns, T., & Bower, R. G. 2013, MNRAS, 429, 1922
Dastidar, R., Misra, K., Singh, M., et al. 2021, MNRAS, 504, 1009
de Avillez, M. A. 2000, MNRAS, 315, 479
de Blok, W. J. G., Walter, F., Brinks, E., et al. 2008, AJ, 136, 2648
Dettmar, R. J. 1990, A&A, 232, L15
Edgar, R. J., & Savage, B. D. 1989, ApJ, 340, 762
Egger, R. J., & Aschenbach, B. 1995, A&A, 294, L25
El-Badry, K., Bradford, J., Quataert, E., et al. 2018, MNRAS, 477, 1536

Farber, R. J., & Gronke, M. 2022, MNRAS, 510, 551
Fielding, D., Quataert, E., & Martizzi, D. 2018, MNRAS, 481, 3325
Foreman-Mackey, D., Hogg, D. W., Lang, D., & Goodman, J. 2013, PASP, 125, 306
Fraternali, F., & Binney, J. J. 2006, MNRAS, 366, 449
Fraternali, F., & Binney, J. J. 2008, MNRAS, 386, 935
Fraternali, F., Marasco, A., Marinacci, F., & Binney, J. 2013, ApJL, 764, L21
Fraternali, F., van Moorsel, G., Sancisi, R., & Oosterloo, T. 2002, AJ, 123, 3124
Gillmon, K., & Shull, J. M. 2006, ApJ, 636, 908
Girichidis, P., Naab, T., Walch, S., & Berlok, T. 2021, MNRAS, 505, 1083
Girichidis, P., Walch, S., Naab, T., et al. 2016, MNRAS, 456, 3432
Green, G. 2018, JOSS, 3, 695
Haffner, L. M., Reynolds, R. J., Tufte, S. L., et al. 2003, ApJS, 149, 405
Hartmann, J. 1904, ApJ, 19, 268
Heckman, T. M., Lehnert, M. D., Strickland, D. K., & Armus, L. 2000, ApJS, 129, 493
Henley, D. B., Shelton, R. L., Kwak, K., Hill, A. S., & Mac Low, M.-M. 2015, ApJ, 800, 102
Heyer, M., & Dame, T. M. 2015, ARA&A, 53, 583
Hobbs, L. M. 1969, ApJ, 158, 461
Hobbs, L. M. 1974, ApJ, 191, 381
Howk, J. C., Rueff, K. M., Lehner, N., et al. 2018, ApJ, 856, 166
Howk, J. C., & Savage, B. D. 1997, AJ, 114, 2463
Howk, J. C., & Savage, B. D. 2000, AJ, 119, 644
Howk, J. C., Sembach, K. R., & Savage, B. D. 2003, ApJ, 586, 249
Jenkins, E. B. 1978, ApJ, 220, 107
Joung, M. K. R., & Mac Low, M.-M. 2006, ApJ, 653, 1266
Kacprzak, G. G., Churchill, C. W., Steidel, C. C., & Murphy, M. T. 2008, AJ, 135, 922
Kacprzak, G. G., Cooke, J., Churchill, C. W., Ryan-Weber, E. V., & Nielsen, N. M. 2013, ApJL, 777, L11
Kado-Fong, E., Kim, J.-G., Ostriker, E. C., & Kim, C.-G. 2020, ApJ, 897, 143
Kalberla, P. M. W., Burton, W. B., Hartmann, D., et al. 2005, A&A, 440, 775
Kalberla, P. M. W., & Kerp, J. 2009, ARA&A, 47, 27
Kamphuis, P., Holwerda, B. W., Allen, R. J., Peletier, R. F., & van der Kruit, P. C. 2007, A&A, 471, L1
Kamphuis, P., Józsa, G. I. G., Oh, S. H., et al. 2015, MNRAS, 452, 3139
Kennicutt, R. C. 1998, ARA&A, 36, 189
Kerp, J., Burton, W. B., Egger, R., et al. 1999, A&A, 342, 213
Kim, C.-G., & Ostriker, E. C. 2018, ApJ, 853, 173
Kim, C.-G., Ostriker, E. C., Somerville, R. S., et al. 2020, ApJ, 900, 61
Korpi, M. J., Brandenburg, A., Shukurov, A., & Tuominen, I. 1999, A&A, 350, 230
Kreckel, K., Faesi, C., Kruijssen, J. M. D., et al. 2018, ApJL, 863, L21
Kulkarni, V. P., Bowen, D. V., Straka, L. A., et al. 2022, ApJ, 929, 150
Kuntz, K. D., & Danly, L. 1996, ApJ, 457, 703
Kuntz, K. D., & Snowden, S. L. 2000, ApJ, 543, 195
Lan, T.-W., Ménard, B., & Zhu, G. 2014, ApJ, 795, 31
Lan, T.-W., & Mo, H. 2018, ApJ, 866, 36
Lanzetta, K. M., & Bowen, D. 1990, ApJ, 357, 321
Lehner, N., & Howk, J. C. 2011, Sci, 334, 955
Li, A., Marasco, A., Fraternali, F., Trager, S., & Verheijen, M. A. W. 2021, MNRAS, 504, 3013
Mac Low, M.-M., & McCray, R. 1988, ApJ, 324, 776
Manuwal, A., Ludlow, A. D., Stevens, A. R. H., Wright, R. J., & Robotham, A. S. G. 2022, MNRAS, 510, 3408
Marasco, A., & Fraternali, F. 2017, MNRAS, 464, L100
Marasco, A., Fraternali, F., & Binney, J. J. 2012, MNRAS, 419, 1107
Marasco, A., Marinacci, F., & Fraternali, F. 2013, MNRAS, 433, 1634
Marasco, A., Fraternali, F., Heald, G., et al. 2019, A&A, 631, A50
Martin, C. L. 2005, ApJ, 621, 227
Martizzi, D., Fielding, D., Faucher-Giguère, C.-A., & Quataert, E. 2016, MNRAS, 459, 2311
McClure-Griffiths, N. M., Pisano, D. J., Calabretta, M. R., et al. 2009, ApJS, 181, 398
Ménard, B., Wild, V., Nestor, D., et al. 2011, MNRAS, 417, 801
Moster, B. P., Naab, T., & White, S. D. M. 2013, MNRAS, 428, 3121
Moustakas, J., Coil, A. L., Aird, J., et al. 2013, ApJ, 767, 50
Munari, U., & Zwitter, T. 1997, A&A, 318, 269
Münch, G., & Zirin, H. 1961, ApJ, 133, 11
Murga, M., Zhu, G., Ménard, B., & Lan, T.-W. 2015, MNRAS, 452, 511
Nielsen, N. M., Churchill, C. W., & Kacprzak, G. G. 2013, ApJ, 776, 115
Norman, C. A., & Ikeuchi, S. 1989, ApJ, 345, 372
Noterdaeme, P., Srianand, R., & Mohan, V. 2010, MNRAS, 403, 906

Oh, S.-H., de Blok, W. J. G., Brinks, E., Walter, F., & Kennicutt, R. C. , J. 2011, AJ, 141, 193

Oh, S.-H., Staveley-Smith, L., Spekkens, K., Kamphuis, P., & Koribalski, B. S. 2018, MNRAS, 473, 3256

Oman, K. A., Marasco, A., Navarro, J. F., et al. 2019, MNRAS, 482, 821

Oosterloo, T., Fraternali, F., & Sancisi, R. 2007, AJ, 134, 1019

Phillips, A. P., Pettini, M., & Gondhalekar, P. M. 1984, MNRAS, 206, 337

Phillips, M. M., Simon, J. D., Morrell, N., et al. 2013, ApJ, 779, 38

Planck Collaboration, Aghanim, N., Ashdown, M., et al. 2016, A&A, 596, A109

Poznanski, D., Prochaska, J. X., & Bloom, J. S. 2012, MNRAS, 426, 1465

Prevot, M. L., Lequeux, J., Maurice, E., Prevot, L., & Rocca-Volmerange, B. 1984, A&A, 132, 389

Prochaska, J. X., Chen, H.-W., Wolfe, A. M., Dessauges-Zavadsky, M., & Bloom, J. S. 2008, ApJ, 672, 59

Prochaska, J. X., & Wolfe, A. M. 1997, ApJ, 487, 73

Prochaska, J. X., Tejos, N., Crighton, N., et al. 2016, linetools/linetools: Second major release, v0.2, Zenodo, doi:10.5281/zenodo.168270

Puspitarini, L., & Lallement, R. 2012, A&A, 545, A21

Rand, R. J., Kulkarni, S. R., & Hester, J. J. 1990, ApJL, 352, L1

Richmond, M. W., Treffers, R. R., Filippenko, A. V., et al. 1994, AJ, 107, 1022

Richter, P. 2017, in Gas Accretion onto Galaxies, ed. A. Fox & R. Davé, Vol. 430 (Cham: Springer International Publishing AG), 15

Richter, P., Krause, F., Fechner, C., Charlton, J. C., & Murphy, M. T. 2011, A&A, 528, A12

Richter, P., Sembach, K. R., Wakker, B. P., & Savage, B. D. 2001a, ApJL, 562, L181

Richter, P., Sembach, K. R., Wakker, B. P., et al. 2001b, ApJ, 559, 318

Roberts-Borsani, G. W., Saintonge, A., Masters, K. L., & Stark, D. V. 2020, MNRAS, 493, 3081

Rogstad, D. H., Lockhart, I. A., & Wright, M. C. H. 1974, ApJ, 193, 309

Röhser, T., Kerp, J., Ben Bekhti, N., & Winkel, B. 2016, A&A, 592, A142

Routly, P. M., & Spitzer, L. J. 1952, ApJ, 115, 227

Rubin, K. H. R., Diamond-Stanic, A. M., Coil, A. L., Crighton, N. H. M., & Moustakas, J. 2018, ApJ, 853, 95

Rubin, K. H. R., Prochaska, J. X., Koo, D. C., et al. 2014, ApJ, 794, 156

Rupke, D. S., Veilleux, S., & Sanders, D. B. 2005, ApJS, 160, 87

Rupke, D. S. N., Gültekin, K., & Veilleux, S. 2017, ApJ, 850, 40

Rupke, D. S. N., Thomas, A. D., & Dopita, M. A. 2021, MNRAS, 503, 4748

Savage, B. D., & Sembach, K. R. 1991, ApJ, 379, 245

Savage, B. D., & Wakker, B. P. 2009, ApJ, 702, 1472

Savage, B. D., Sembach, K. R., Wakker, B. P., et al. 2003, ApJS, 146, 125

Schlafly, E. F., & Finkbeiner, D. P. 2011, ApJ, 737, 103

Schlegel, D. J., Finkbeiner, D. P., & Davis, M. 1998, ApJ, 500, 525

Schneider, D. P., Hall, P. B., Richards, G. T., et al. 2007, AJ, 134, 102

Schwartz, C. M., & Martin, C. L. 2004, ApJ, 610, 201

Sembach, K. R., & Danks, A. C. 1994, A&A, 289, 539

Sembach, K. R., Danks, A. C., & Savage, B. D. 1993, A&AS, 100, 107

Shapiro, P. R., & Field, G. B. 1976, ApJ, 205, 762

Sheinis, A. I., Bolte, M., Epps, H. W., et al. 2002, PASP, 114, 851

Smith, N., & Andrews, J. E. 2020, MNRAS, 499, 3544

Smoker, J. V., Keenan, F. P., & Fox, A. J. 2015, A&A, 582, A59

Stocke, J. T., Case, J., Donahue, M., Shull, J. M., & Snow, T. P. 1991, ApJ, 374, 72

Straka, L. A., Whichard, Z. L., Kulkarni, V. P., et al. 2013, MNRAS, 436, 3200

Straka, L. A., Noterdaeme, P., Srianand, R., et al. 2015, MNRAS, 447, 3856

Swaters, R. A., van Albada, T. S., van der Hulst, J. M., & Sancisi, R. 2002, A&A, 390, 829

Taylor, E. N., Hopkins, A. M., Baldry, I. K., et al. 2011, MNRAS, 418, 1587

Tenorio-Tagle, G., & Bodenheimer, P. 1988, ARA&A, 26, 145

Thom, C., Putman, M. E., Gibson, B. K., et al. 2006, ApJL, 638, L97

Tomisaka, K., & Ikeuchi, S. 1986, PASJ, 38, 697

Tumlinson, J., Oey, S., Henry, A., et al. 2019, BAAS, 51, 380

Vallerga, J. V., Vedder, P. W., Craig, N., & Welsh, B. Y. 1993, ApJ, 411, 729

van der Hulst, T., & Sancisi, R. 1988, AJ, 95, 1354

van der Wel, A., Franx, M., van Dokkum, P. G., et al. 2014, ApJ, 788, 28

Veilleux, S., Cecil, G., & Bland-Hawthorn, J. 1995, ApJ, 445, 152

Veilleux, S., Maiolino, R., Bolatto, A. D., & Aalto, S. 2020, A&ARv, 28, 2

Vijayan, A., Kim, C.-G., Armillotta, L., Ostriker, E. C., & Li, M. 2020, ApJ, 894, 12

Wakker, B. P. 2001, ApJS, 136, 463

Wakker, B. P., & van Woerden, H. 1991, A&A, 250, 509

Wakker, B. P., York, D. G., Wilhelm, R., et al. 2008, ApJ, 672, 298

Wakker, B. P., York, D. G., Howk, J. C., et al. 2007, ApJL, 670, L113

Wang, J., Koribalski, B. S., Serra, P., et al. 2016, MNRAS, 460, 2143

Wang, J., Kauffmann, G., Józsa, G. I. G., et al. 2013, MNRAS, 433, 270

Watts, A. B., Power, C., Catinella, B., Cortese, L., & Stevens, A. R. H. 2020, MNRAS, 499, 5205

Weiner, B. J., & Williams, T. B. 1996, AJ, 111, 1156

Welty, D. E., Federman, S. R., Gredel, R., Thorburn, J. A., & Lambert, D. L. 2006, ApJS, 165, 138

Welty, D. E., Morton, D. C., & Hobbs, L. M. 1996, ApJS, 106, 533

Welty, D. E., Xue, R., & Wong, T. 2012, ApJ, 745, 173

Werk, J. K., Prochaska, J. X., Thom, C., et al. 2013, ApJS, 204, 17

Werk, J. K., Rubin, K. H. R., Bish, H. V., et al. 2019, ApJ, 887, 89

Westfall, K. B., Cappellari, M., Bershady, M. A., et al. 2019, AJ, 158, 231

Wild, V., & Hewett, P. C. 2005, MNRAS, 361, L30

Wild, V., Hewett, P. C., & Pettini, M. 2007, MNRAS, 374, 292

Womble, D. S., Junkkarinen, V. T., Cohen, R. D., & Burbidge, E. M. 1990, AJ, 100, 1785

Yao, Y., Tripp, T. M., Wang, Q. D., et al. 2009, ApJ, 697, 1784

York, D. G., Adelman, J., Anderson, J. E., et al. 2000, AJ, 120, 1579

York, D. G., Khare, P., Vanden Berk, D., et al. 2006, MNRAS, 367, 945

York, D. G., Straka, L. A., Bishof, M., et al. 2012, MNRAS, 423, 3692

Zheng, Y., Peek, J. E. G., Werk, J. K., & Putman, M. E. 2017, ApJ, 834, 179

Zhu, G., & Ménard, B. 2013, ApJ, 773, 16

Zschaechner, L. K., & Rand, R. J. 2015, ApJ, 808, 153

Zych, B. J., Murphy, M. T., Hewett, P. C., & Prochaska, J. X. 2009, MNRAS, 392, 1429

Zych, B. J., Murphy, M. T., Pettini, M., et al. 2007, MNRAS, 379, 1409